Electro-Chemo-Mechanical Induced Fracture Modeling in Proton Exchange Membrane Water Electrolysis for Sustainable Hydrogen Production

Fadi Aldakheel [1a,b], Chaitanya Kandekar[c], Boris Bensmann[d], Hüsnü Dal[e], Richard Hanke-Rauschenbach[d]

[a]*Institute of Continuum Mechanics, Leibniz Universität Hannover, 30823 Garbsen, Germany;*
[b]*Department of Mechanical Engineering, Faculty of Science and Engineering, Swansea University, Bay Campus, SA1 8EN, UK*
[c]*Helmut Schmidt University / University of the Federal Armed Forces Hamburg, Chair of Structural Analysis, Hamburg, Germany*
[d]*Institute of Electric Power Systems, Electric Energy Storage Systems Section, Leibniz Universität Hannover, Germany*
[e]*Department of Mechanical Engineering, Middle East Technical University, Ankara 06800, Turkey*

Abstract

This work provides a framework for predicting fracture of catalyst coated membrane (CCM) due to coupled electro-chemo-mechanical degradation processes in proton exchange membrane water electrolysis (PEMWE) cells. Electrolysis in the catalyst layer (CL) bulk, diffusion of Hydrogen proton through the membrane (MEM), and mechanical compression at the interface with the porous transport layer (PTL) *generate micro-cracks* that influence the catalyst degradation. Based on our experimental observations, we propose a new theoretical formulations along with the constitutive framework to help understanding and providing a reliable description of the stated multi-physics problem. The computational modeling of crack formation in the CL bulk is achieved in a convenient way by continuum phase-field formulations to fracture, which are based on the regularization of sharp crack discontinuities. The model performance is demonstrated through two representative boundary value problems, representing the cell setup and working of the PEMWE cell.

Keywords: Sustainable Hydrogen Production; Proton Exchange Membrane Water Electrolysis (PEMWE); Catalyst Coated Membrane (CCM); Porous Transport Layer (PTL); Multi-Physics Problem; Experimental Observations.

1. Introduction

Following the Climate Protection Law, the European Union (EU) is targeting net-zero greenhouse gas emissions by 2050 [94; 31]. To meet the EU climate goals, cleaner and renewable energy sources combined with innovative technologies are required [69]. The key driver for accelerating such energy transition is the process of producing green Hydrogen (H_2) from water-electrolysis due to its role in advancing decarbonization sectors.

H_2 is number one in the periodic table, the lightest element, the most frequently found in the universe and has what it take to save the climate. We can produce green H_2 from electricity generated using renewable completely climate neutral. H_2 is a major player in decarbonisation sectors, due to its role in the energy transition from a fossil fuel to a renewable based energy system. As an advantage, it delivers a zero-carbon raw material for a wide range of industries as well as zero-carbon energy to generate heat and electricity for cars, trains and airplanes running on fuel cells. In order to accelerate Hydrogen production for an eco-friendly economy, further development of skills is inescapable.

Water electrolysis being the major contributor to high-quality Hydrogen production with relatively high efficiency ($\sim 70\%$) [23], has been studied and continuously developed over the past decades. Among all the types of electrolysis methods, Polymer Electrolyte Membrane (also known as proton exchange membrane) water electrolysis have recently received considerable attention due to the possibility of achieving higher efficiencies [61]. A typical water electrolysis

[1]Corresponding author: Fadi Aldakheel (Leibniz Universität Hannover & Swansea University).

Web: https://www.ikm.uni-hannover.de/de/aldakheel

E-mail addresses: aldakheel@ikm.uni-hannover.de || fadialdakheel@googlemail.com (F. Aldakheel); kandekarchaitanya@hsu-hh.de (C. Kandekar); boris.bensmann@ifes.uni-hannover.de (B. Bensmann); dal@metu.edu.tr (H. Dal); hanke-rauschenbach@ifes.uni-hannover.de (R. Hanke-Rauschenbach).

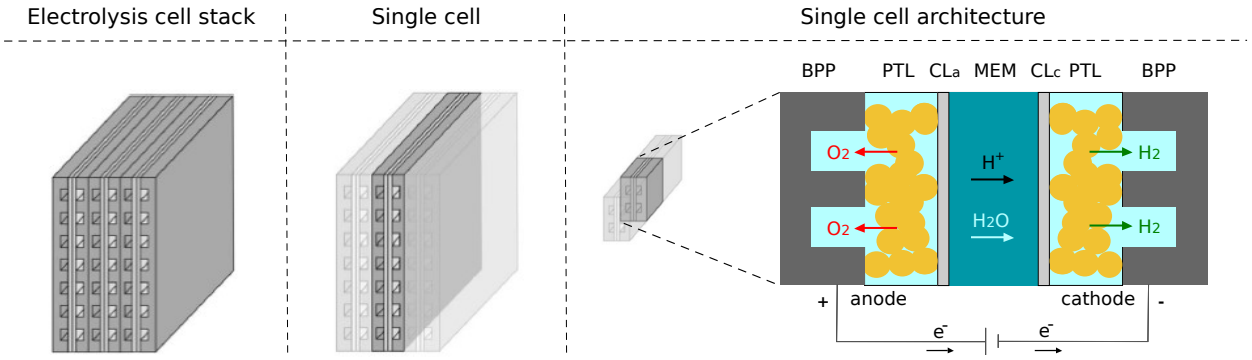

Figure 1: PEM water electrolyzers: Schematic description of an electrolysis cell stack, in line with [97]. The electrolysis cell consists of membrane (MEM) coated with cathodic and anodic catalyst layer (CLs) sandwiched between two porous transport layers (PTLs) and bipolar plates (BPPs) with flow channels.

using polymer electrolyte membrane (PEM) consists of anode, cathode, current collector - bipolar plates (BPP), porous transport layer (PTL), catalyst layer (CL) and membrane (MEM) as schematically plotted in figure 1. In the PEMWE cell, water flows from the anode towards the cathode side and is electrolysed in the CL_a layer due to the application of voltage ($E_{rev} \sim 1.23V$). Thereafter, O_2 is produced and collected at the anode while protons are transported through the solid membrane towards the cathode. Next, H_2 is produced and collected at the cathode as demonstrated in figure 1. For oxygen evolution reaction (OER) at the anode, iridium oxide (IrO_2) or ruthenium oxide (RuO_2) is used as a catalyst [23; 84]. On the other hand, for Hydrogen evolution reaction (HER), platinum (Pt) is typically used as a catalyst. The perflurosulphonic acid as an electrolyte is used in a solid sulfonated polystyrene membrane. In this regard, protons are generated and transported through the CL_a/MEM/CL_c section of the electrolysis cell, which couples the electro-chemistry and diffusion mechanics. The electrochemical potential across the cell drives protons to flow from one electrode to another, whereas electrons complete the circuit by flowing through an external electronic conductor.

In PEMWE cell, the PTL structure, catalyst morphology, structural integrity of membrane, external mechanical compression, cell temperature and pressure, and transport mechanisms (water-, electric- and ionic-transport) play the main roles in cell performance. Water transport mechanisms can be controlled with controlling the water flow rate, which guarantees the feed supply for the reaction and homogenize the temperature distribution. This behavior was studied under various conditions by Immerz et al. [43]. Electric transport is governed by Ohm's law, wherein protons and electrons are only produced/consumed in the catalyst layers. In this transport mechanism, exchange current density, catalyst surface, tortuosity, temperature and water present in ionomer are the influencing parameters, see Springer et al. [87] and Trinke [95]. In ionic transport, Hydrogen proton transport is the most important phenomena. In literature, there are many explanations of proton transport mechanisms within CLs and MEM. Critical examination and analysis of recently proposed and classical models for proton transport mechanism are described in Fimrite et al. [34]; Babic [15]; Babic et al. [16]. In transport mechanisms, concentration and pressure fields are among the influencing factors that can be mathematically modeled for PEM, see Grigoriev et al. [36]. Hydrogen proton transport within the catalyst layers is dependent on the ionomer content and network [96], catalyst material, catalyst thickness and loading [16], deformation of catalyst due to external mechanical pressure [18; 52; 67], and catalyst degradation etc. Regarding catalyst materials, the usage of noble metals such as iridium and platinum as a catalyst in CCM has been a major concern due to better utilisation and electrochemical stability of the catalyst [14; 51]. The influence of cell compression on catalyst layers in water electrolysis cells has been strongly discussed in the electrolysis community, academia as well as industry. In this regard, effects of thickness and loading of catalyst were studied by [16]. In this study, thicker CLs resulted in longer diffusion distance for the reactant and yielded inhomogenous water distribution in CL. In Babic et al. [17] effects of PTL/CL_a interface on the cell characteristics were investigated. Therein, it was shown that the CL_a area under the solid PTL particle is compressed and local porosity is reduced. Thereby, during the proton transport in compacted CL_a, which contributes to OER, water reaches CL_a through the voids on the PTL surface and relies on the lateral diffusion through the ionomer binder to reach the active sites under the PTL solid particles.

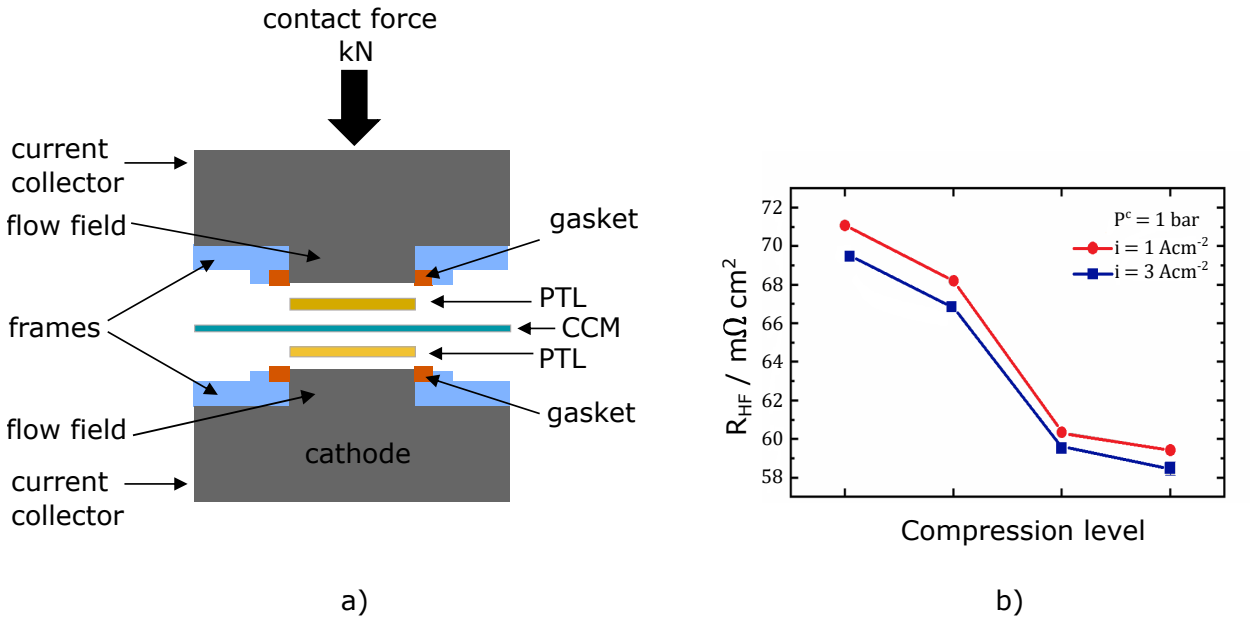

Figure 2: PEMWE experimental step-up (adopted from authors work [52]) for different compression levels: a) Schematic representation of the cell as used in the Leibniz Universität Hannover authors-lab; b) dependence of the high frequency resistance R_{HF} at 1 $A\ cm^{-2}$ (red) and 3 $A\ cm^{-2}$ (blue) on the compression level at cathode pressure $p^c = 1\ bar$.

Following the Leibniz Universität Hannover researchers work [52], a typical cell setup of an electrolysis cell is intensively discussed and depicted in Figure 2a. Most important for understanding the problem is looking at the interplay between the cell compression, adjusted by the contact force, the flow field structures, the gas and water diffusion media (PTLs), and finally the catalyst coated membrane (CCM) in the middle of the sandwich. The cell has to be compressed to keep it gas tight and to decrease the contact resistances within the sandwich. Figure 2b shows the effect of different compression levels on the cells high frequency resistance as representative of the ohmic cell resistance. It can be reduced by increasing the contact force. Figure 3 illustrates experimental outcomes of a joint-research between HySA Catalysis (Hydrogen South Africa) and our Leibniz Universität Hannover team. From the close observation, it becomes clear that the fibers of the porous transport layers penetrate into the catalyst layer. The penetration depth also depends on the cell compression. This has an effect on the morphology of the catalyst layer, which needs further investigations, see figure 2. In a similar direction, Babic et al. [18] evaluated morphological changes in the CL due to excess external mechanical compression and its effects on the cell performance. As expected, CCM was compressed by PTL particles and found to be creeped into PTL voids under cell clamping force. Furthermore, deformed catalysts led to breaks in proton transport network and cells with more clamping pressure resulted into higher degradation rates. On the one hand, mechanical cell compression increases catalyst surface contact and thus the cell performance; on the other hand, excess mechanical pressure can damage the CL and it will result in crack formation in the PTL void region. Regarding catalyst degradation, many researchers observed different degradation mechanisms such as the rate of electro-chemical water-splitting reaction in the CL bulk, weak micro-porous structure of the catalyst, initial catalyst damage due to excess mechanical pressure, and also anisotropic swelling and fracture of the membrane in both directions. Micro-cracks formed due to complicated multi-physics phenomenon are investigated in Schuler et al. [80]. In line with the experimental setup and its finding, shown in figures 2 and 3 respectively, catalyst deformation due to cell assembly and degradation due to complicated coupled processes can be modeled and visualized in figure 4. Presence of many dependent parameters makes catalyst degradation a complicated and one of the less understood process. Effects on the transport mechanisms due to external mechanical pressure highlight the importance of the structural design of the PTL/CL and their interfaces along with the cell assembly procedure. This demands new advanced physical and electrochemical characterization tools to fundamentally and deeply understand (i) the mechanism of electrolysis reaction (HER and OER), (ii) the electro-chemo-mechanical interactions of current collector - catalyst - membrane (PTL/CL/MEM) along with their relationship with other cell components, and (iii) the multi-phase transport model

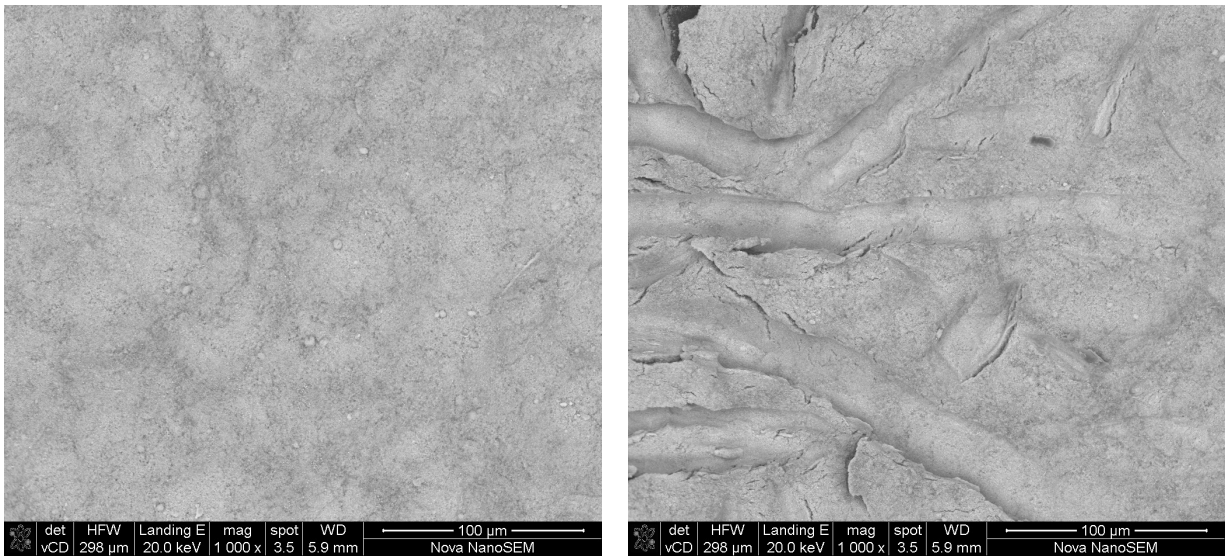

Figure 3: Top view of a catalyst layer: Single fibres of the porous transport layers penetrate into the catalyst layer. The images result from the same catalyst layer, showing an affected (right) and unaffected area (left). (Images source: `www.hysacatalysis.uct.ac.za` in cooperation with Leibniz Universität Hannover team).

for tailoring the operating parameters to raise the performance, especially for large scale electrolyzers. Representative experimental works to understand inter-dependencies of parameters and their synergistic effects are proposed by Babic et al. [16, 18]; Bueler et al. [22]; De Angelis et al. [27]; Garbe et al. [35]; Immerz et al. [44, 45]; Ito et al. [46]; Liso et al. [50]; Rozian & P.Millet [72]; Papakonstantinou et al. [67]; Schmidt et al. [75]; Schuler et al. [78, 80]; Siracusano et al. [86]; Tanaka et al. [92, 93]; Trinke et al. [96]; Trinke [95]; Yu et al. [105].

Based on the above observations, hot topics in PEMWE research are: optimizing the morphology of catalyst layers, increasing catalyst utilisation, reducing the catalyst dependency on noble metals, optimizing structural design of PTL and CL, improving water transport mechanisms, increasing long term durability of all components, and improving membrane characteristics and developing stack concepts, to mention but a few [14; 23; 99]. In this context, analyzing the *failure behavior* within the catalyst layers of proton exchange membrane water electrolysis (PEMWE) cells is an essential task. These interfaces control the catalyst utilization and over-potentials, hence influencing the electrochemical conversion performance or the system efficiency. Hereby basic understanding is still missing, which geometrical and/or transport properties are important and how they affect the individual over-voltages. In this work, advanced computational modeling framework across various disciplines and scales combined with fracture mechanics are developed towards enhancing the reliability, durability and performance of Hydrogen technologies.

The computational modeling of crack propagation can be achieved in a convenient way by the continuum phase-field approach to fracture, which is based on the regularization of sharp crack discontinuities. Due to its simplicity,

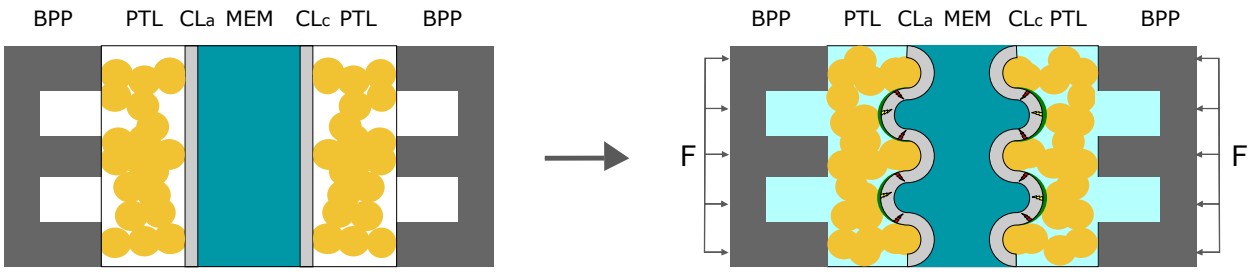

Figure 4: PEM water electrolyzer cell setup. Left: Assembly of all cell components; and right: operating cell with applied external compressive forces and feed water showing microscopic deformations and crack developments in catalyst layers.

this methodology has gained wide interest by the engineering community since 2008. From there on many scientists have worked in this field and developed phase-field approaches for finite elements, isogeometric analysis, and lately also for the virtual element technology. The main driving force for these developments is the possibility to handle complex fracture phenomena within numerical methods in two and three dimensions. In recent years, several brittle [20; 59; 42; 41; 71; 7; 30; 39; 76; 88; 13; 33; 6; 100; 68; 40; 70; 82; 62; 11; 107; 81; 1; 91; 66; 19; 29; 38; 103] and ductile [64; 10; 4; 8; 83; 24; 32; 48; 63; 28; 9; 5; 21; 89; 98; 47; 65; 77] phase-field fracture formulations have been proposed in the literature. These studies range from the modeling of 2D/3D small and large strain deformations, variational formulations, multi-scale/physics problems, mathematical analysis, different decompositions, and discretization techniques with many applications in science and engineering. Recently, the phase-field approach has been extended towards Hydrogen assisted cracking, see Martínez-Pañeda et al. [53]; Cui et al. [25]. All these examples and the citation therein demonstrate the potential of phase-field for crack propagation.

Contribution regarding the numerical implementation of electro-chemo-mechanical response in multi-physics problems is given by Zohdi [109, 108]; Zohdi & Wriggers [111]; Zohdi & Meletis [110] and in Wu & Lorenzis [102] using Fickian diffusion. Furthermore, chemical diffusion using Cahn-Hilliard reaction coupled with finite elasticity is explained in Anand [12]; Dal & Miehe [26]; Leo et al. [49]; Miehe et al. [55, 58, 57, 54]. In the present contribution, we developed a coupled electro-chemo-mechanical induced fracture model in Proton Exchange Membrane Water Electrolysis (PEMWE) Cells. Hereby, the main framework includes a finite strain theory for chemo-elasticity coupled with phase-field fracture, which provides a reliable description of the stated multi-physics problem. An extended Cahn-Hillard type diffusion for possible phase segregation of Hydrogen ions is incorporated in the model, which is based on C_0 continuous basis functions. Interaction of the chemo-mechanical process with the electrical field enters the formulation in terms of Butler-Volmer kinetics for the surface reactions. Regarding the material failure, the phase-field model, a geometric approach for diffusive crack modeling, is applied with irreversibility based on Griffith criteria G_c. This methodology is exploited in the numerical implementation by constructing a robust finite element method with algorithmic decoupling for fracture. The fracture response of the catalyst layer in CCM is analyzed in two-staged boundary value problem to understand the contribution of individual process in the complex phenomenon. Furthermore, this study would give a reliable description of the interaction between electro-chemo-mechanical aspects, which can be exploited for the optimization of control parameters such as mechanical pressure and externally applied voltage to increase the catalyst efficiency.

The paper is organized as follows: Section 2 outlines the fundamentals of PEMWE cell to describe the complexity of the real problem along with the necessary assumptions to simplify the problem. In section 3, the governing equations for the coupled problem are described. Next, the weak formulations are derived in Section 4. This also includes a distinct structure of balance equations and their algorithmic implementation to calculate the bulk response using the finite element method (FEM). Finally, some numerical tests are carried out to substantiate our algorithmic developments in Section 5.

2. Fundamentals of PEMWE cells

In this section, fundamentals and state-of-the-art information regarding proton exchange membrane water electrolysis (PEMWE) cells are described to help understanding involved crucial physical processes. In order to formulate boundary value problem of the coupled problem, the modeling strategy is presented with the model assumptions.

2.1. Working principle and cell performance

Typical setup of PEMWE single cell is demonstrated in figure 1. The cell consists of a symmetric assembly BPP-PTL-CL_a-MEM-CL_c-PTL-BPP. The BPP layer supports the cell as a mechanical structural backup and presses the stack homogeneously to increase the contact area. The PTLs main contribution in the cell is the transportation of current, water and gas mixtures along with the mechanical support of the CCM. The CLs are the critical components in the cell, which consists of catalyst particles. Herein, electro-chemical reaction take place in those particles during the oxidation and reduction reactions, and the transport of electrons. In the catalyst layer, the feed water and generated gases are transported through its pores to other sides. The PEM membrane at the center of the cell separates the cell into two half-cells viz. anode and cathode side half cell with its properties of gas impermeability and electrical insulation. The main task here is to transport protons from the anode to the cathode catalyst layer.

In order to set up the PEMWE cell, first all cell components are arranged in order stated above. Then, external mechanical pressure is applied to hold the components all together. To initiate the cell operation, anode is fed with deionized (DI) water which flows from BPP towards PTL. The cell is then switched to a potentiostatic or galvanostatic mode of operation. In potentiostatic operation, voltage is applied to the electrodes which initiates the cell operations. On the other hand, in the galvanostatic method, the current is controlled which governs the cell output. Therefore, upon application of electricity (and heat), at anode side water is oxidized (Oxygen Evolution Reaction) to produce O_2, protons and electrons. Thereafter, protons are conducted through the membrane towards cathode where it reduces (Hydrogen Evolution Reaction) to form H_2. Produced gases at the anode and the cathode sides are collected through respective PTLs. In PEMWE cell operation, both potentiostatic and galvanostatic methods are initiated by setting desired operating point. The operating point, defines the pressure, temperature and local current density. Once the operating point is selected it reaches the steady-state slowly. Then, overvoltages become stable with respect to time when it achieves the steady-state. Complete PEMWE cell reaction can be written as

$$H_2O_{(l)} + 237.2 \text{ kJ mol}^{-1} + 48.6 \text{ kJ mol}^{-1} \rightarrow H_2 \ + \ \frac{1}{2}O_2 \ . \tag{1}$$

In the above equation, liquid water is converted to Hydrogen and oxygen with externally supplied electrical energy of 237.2 $kJmol^{-1}$ and heat energy of 48.6 $kJmol^{-1}$, respectively. Reaction at the anode side represents oxygen evolution reaction (OER) and stated as

$$H_2O_{(l)} \rightarrow 2H^+ \ + \ \frac{1}{2}O_2 \ + \ 2e^-, \tag{2}$$

and reaction at the cathode, also called as Hydrogen evolution reaction (HER), is given by

$$2H^+ \ + \ 2e^- \rightarrow H_2. \tag{3}$$

The cell efficiency η_{cell} can be computed as a product of voltage efficiency η_E and Faradays efficiency η_{H_2} as

$$\eta_{cell} = \eta_E \cdot \eta_{H_2} \quad \text{with} \quad \eta_E = \frac{E^0}{E_{cell}} \quad \text{and} \quad \eta_{H_2} = \frac{N_{H_2}^{c,out}}{N_{H_2}^{theo}}. \tag{4}$$

Here, E^0 is the reversible cell voltage, E_{cell} is the cell voltage, $N_{H_2}^{c,out}$ is the actual molar flux at the cathode output and $N_{H_2}^{theo}$ is the theoretical molar flux. The cell voltage E_{cell} is calculated as a function of three over-potentials, namely kinetic over-potential η_{kin}, electric over-potential η_Ω and mass transport over-potential η_{mtx}. Total cell potential loss is the summation of all three over-potentials and these are the key factors affecting cell performance. Therefore, cell voltage is calculated as,

$$E_{cell} = E^0(p, T) + \eta_{kin} + \eta_\Omega + \eta_{mtx} \ . \tag{5}$$

Along with the necessary cell over-potentials, pressure and temperature affect the cell performance greatly. For pressurized operations, two modes of operations are used, namely balanced and differential based on the pressures on Hydrogen and oxygen side. Hence, operating conditions in the PEMWE cell setup (e.g. pressure, temperature and current density) are determinant of cell performance degradation and efficiency. In this way, cell performance can be measured by using the above equations and operating point can be controlled to reduce cell losses, further details are explained in Schmidt et al. [75] and Trinke [95].

2.2. Degradation phenomena in catalyst layer

Deformation and fracture of the catalyst layers depend on external mechanical loading, cell temperature, membrane humidity, gas crossover phenomenon, liquid water pressure, feed water purity, heat generation and local current density. It is critical to monitor essential components such as PTL and CCM in order to enhance or scale up the performance of the cell. Scientific works to understand the PTL/CCM interaction and degradation of CL in PEMWE is scarce as compared to the study of the fuel cell. From the available literature, it can be highlighted that CCM degradation is mainly due to chemical, mechanical, and thermal stresses along with the loss of functional group due to oxidation. Therein, chemical degradation is caused by gradual decomposition due to the oxidation by radicals viz. Hydroxyl, Hydroperoxyl, Hydrogen peroxide. To this end, feed water purity can be important factor for ion poisoning.

Since most of the system components are made of stainless steel, its metallic cations get dissolved in the deionized feed water. These dissolved cations of Fe, Cu and Ca contaminate the CCM and result in ion poisoning. Furthermore, it reduces the overall performance of the PEMWE with time, which has significant effects on the anode side than cathode part [15]. This degradation can be controlled by maintaining the high purity of the feed water.

Regarding mechanical and thermal degradation, excessive mechanical compression from PTL on CCM causes lasting morphological changes and damage in the catalyst area during cell construction. Structural integrity and Young's modulus of the CCM are also reduced when the cell temperature is high [46]. Moreover, chemical and mechanical properties of the CCM are degraded with respect to time due to temperature, humidity and creep. In the literature, many scanning electron microscope (SEM) images of the damaged CL following the electrolyzer operations have been published and examined e.g. Babic [15]; Martin et al. [52].

2.3. Mechanism of proton transport

In order to model electro-chemical process in PEMWE cell, different transport mechanisms for PEM are explored to formulate the correct boundary value problem. Chemical concentration gradients, pressure gradients, humidity, and temperature influence Hydrogen proton transport across the membrane.

Many models are used in the literature to explain membrane transport mechanisms depending on the driving forces. Since the membrane is impervious to gases, only dissolved liquid water may pass through it. Water, together with dissolved Hydrogen and oxygen, is dissolved inside the ionomer that is exclusively found within the membrane and transported over the through-plane direction. Therefore, proton transport is primarily influenced by water and ionomers. The quantity of sorbed waters per sulphonate group head present in the ionomer is called water content (λ), in other words the amount of dissolved water in an ionomer. Water content determines the membrane's conductivity. In general, one can assume that λ has a homogeneous field and that no gradients exist across the membrane. Pressure, chemical concentration, and chemical potential are the three main driving forces that explain membrane transport. The hydraulic model, diffusion model, and TMT model can explain the transport phenomenon in relation to each driving factor respectively [34]. One H_2O molecule per proton is pulled across the membrane during proton transport. The Hydrogen proton is carried in water as an associated species and can diffuse in two ways: Structural diffusion and vehicle diffusion [34]. Hydrogen proton is transported in various ion configurations. Hydronium ion $(H_3O)^+$, Zundel ion $(H_5\ O_2)^+$, and Eigen ion $(H_9\ O_4)^+$ are three distinct ion configurations that can be found in bulk water in the membrane. These three ion configurations have an impact on many transport mechanisms, including bulk water transport, proton conductivity, and electro-osmatic drag, which affects the PEMWE cell's overvoltage and efficiency.

Water content in the membrane can also influence in choosing correct transport model. For example, at saturated membrane conditions, a hydraulic model based on pressure gradient theory is applied; at low water content, the diffusion model based on the proton concentration gradient is preferred. At low water content in the membrane, standard diffusion theory is sufficient to describe the diffusion model. However, there are two kinds of diffusion phenomena: positive and negative diffusion. Positive diffusion occurs when molecules move in the opposite direction of the concentration gradient, lowering the gradient. Positive diffusion is propelled by the concentration gradient. Negative diffusion, on the other hand, occurs in the same concentration gradient direction [85]. As a result, the concentration gradient does not act as a driving force for negative diffusion. Hence, the driving force in the negative diffusion scenario is the gradient of the chemical potential, according to Cahn and Hilliard theory. The decision to choose diffusion modeling theory depends on the equilibrium state. Positive diffusion has an equilibrium state that is a homogeneous mixture, whereas negative diffusion has an equilibrium state that is a two-phase system separated by a fluid interface, which is the case of water-splitting. Hence, in the presented contribution we choose Cahn-Hilliard theory with negative diffusion mechanism to model the electro-chemical process.

The demonstration of phase separation and the need for adopting Cahn-Hilliard diffusion theory comes from a water splitting reaction that occurs within catalyst layer and produces protons and other ions. In this study, transport of only Hydrogen proton is considered, since this represents the key function of PEMWE cells.

2.4. Modeling approach for the multi-physics problem

Degradation at the CCM bulk can be modeled by employing some simplifications and assumptions. Multi-physics interactions of all these phenomena is a tedious task that can be achieved through the correct PEMWE cell model and correct boundary conditions. In what follows are the PEMWE cell assumptions and simplified model formulation in this work:

1. Pressure and temperature are constant throughout the process i.e. $p = 1$ bar and $\theta = 80°$C.
2. Phase separation by the water-splitting reaction and gas crossover phenomena not considered yet for simplicity.
3. Generation and diffusion of only H^+ protons are modeled, while other chemical species are neglected.
4. Diffusion of the H^+ proton is governed by the Cahn-Hilliard negative diffusion mechanism with the gradient of the chemical potential as the driving force.

The Hydrogen proton transport though the CCM bulk will be modeled using the Cahn-Hilliard diffusion equation. Note that, our emphasis in this paper is on (i) *demonstrating the constitutive framework*, and (ii) *highlighting the influence of elector-chemo-mechanically induced damage mechanics* of our proposed CCM model at the microscale. Thus, the formulation performance will be demonstrated utilizing some representative examples representing an experimental procedure for PEMWE cell.

3. Governing equations for the multi-field problem

This section presents the theoretical and numerical frameworks of the electro-chemical and mechanical responses of the catalyst coated membrane component in PEMWE cell along with the catalyst layer failure behavior using the phase-field approach to fracture.

3.1. Basic kinematics and constitutive formulation

Consider a solid $\mathcal{B}_0 \in \mathcal{R}^3$ to be in Lagrangian i.e. reference configuration of the CCM bulk at time $t \in \mathcal{T} = [0, \mathfrak{T}]$ with surface boundary $\partial\mathcal{B}_0$. The coupled multi-field problem can be prescribed by the deformation field of the CCM bulk $\boldsymbol{\varphi}$, phase-field fracture d

$$\boldsymbol{\varphi} : \begin{cases} \mathcal{B}_0 \times \mathcal{T} \to \mathcal{B}_t \in \mathcal{R}^3 \\ (\boldsymbol{X}, t) \mapsto \boldsymbol{x} = \boldsymbol{\varphi}(\boldsymbol{X}, t) \end{cases} , \quad d : \begin{cases} \mathcal{B}_0 \times \mathcal{T} \to [0, 1] \\ (\boldsymbol{X}, t) \mapsto d(\boldsymbol{X}, t) \end{cases} , \tag{6}$$

and the normalized concentration c of the Hydrogen proton (H^+) which diffuses through the CCM along with its chemical potential field μ as

$$c : \begin{cases} \mathcal{B}_0 \times \mathcal{T} \to [0, 1] \\ (\boldsymbol{X}, t) \mapsto c(\boldsymbol{X}, t) \end{cases} , \quad \mu : \begin{cases} \mathcal{B}_0 \times \mathcal{T} \to \mathcal{R} \\ (\boldsymbol{X}, t) \mapsto \mu(\boldsymbol{X}, t) \end{cases} . \tag{7}$$

The deformation $\boldsymbol{\varphi}(\boldsymbol{X}, t)$ maps the points from the reference configuration $\boldsymbol{X} \in \mathcal{B}_0$ to the points in current configuration $\boldsymbol{x} \in \mathcal{B}_t$. The location of the material point in the deformed configuration is defined as $\boldsymbol{x} = \boldsymbol{X} + \boldsymbol{u}(\boldsymbol{X}, t)$, where $\boldsymbol{u}(\boldsymbol{X}, t)$ is the displacement field. The phase-field variable $d(\boldsymbol{X}, t) = 0$ represents the intact and $d(\boldsymbol{X}, t) = 1$ represents fractured state of the catalyst layer bulk along with the irreversibility condition $\dot{d} \geq 0$. The H^+ normalized concentration field $c \in [0, 1]$ is a fraction of the total chemical reference concentration c_{max}. Herein, $c = 0$ depicts no diffusion of H^+ protons in the reference bulk volume of BVP geometry, whereas $c = 1$ reflects the maximum concentration i.e. c_{max} in the cell environment. Physical meaning of the proton concentration evolution is explained in the boundary value problems for catalyst layers at the anode and cathode sides, see section 5.

The gradients of the material deformation, the H^+ concentration and its dual potential driving field are given as

$$\boldsymbol{F} = \nabla\boldsymbol{\varphi}(\boldsymbol{X}, t), \quad \mathbb{C} = \nabla c(\boldsymbol{X}, t) \quad \text{and} \quad \mathbb{M} = -\nabla\mu(\boldsymbol{X}, t) \, , \tag{8}$$

respectively. The deformation gradient, its cofactor and the Jacobian

$$d\boldsymbol{x} = \boldsymbol{F} d\boldsymbol{X}, \quad d\boldsymbol{a} = \operatorname{cof}\boldsymbol{F} d\boldsymbol{A}, \quad dv = \det\boldsymbol{F} dV \tag{9}$$

are used for line, area and volume mappings between reference and current configurations, respectively. To ensure the non-penetrable deformation, the constraint condition is applied on the deformation map $\boldsymbol{\varphi}$ such as $J = det(\boldsymbol{F}) > 0$. Furthermore, the right and left Cauchy-Green tensors read

$$\boldsymbol{C} = \boldsymbol{F}^T\boldsymbol{F} \quad \text{and} \quad \boldsymbol{b} = \boldsymbol{F}\boldsymbol{F}^T \, . \tag{10}$$

Cauchy's stress theorem defines the traction depending linearly on outward surface normal $\boldsymbol{n}$ with Cauchy stress tensor as,

$$\boldsymbol{t} = \boldsymbol{\sigma}(\boldsymbol{x}, t) \cdot \boldsymbol{n} \,. \tag{11}$$

The spatial force $\boldsymbol{t}da$ is scaled to the respective area from reference configuration as $\boldsymbol{T}dA = \boldsymbol{t}da$. This induces unsymmetric 1^{st} Piola-Kirchhoff stress tensor $\boldsymbol{P}$, symmetric Lagrangian 2^{nd} Piola-Kirchhoff stress tensor $\boldsymbol{S}$ and Kirchoff stress $\tilde{\boldsymbol{\sigma}}$ as,

$$\boldsymbol{P} = \tilde{\boldsymbol{\sigma}}\boldsymbol{F}^{-T} \quad \text{and} \quad \boldsymbol{S} = \boldsymbol{F}^{-1}\boldsymbol{P} = \boldsymbol{F}^{-1}\tilde{\boldsymbol{\sigma}}\boldsymbol{F}^{-T} \quad \text{with} \quad \tilde{\boldsymbol{\sigma}} = J\boldsymbol{\sigma} \,. \tag{12}$$

For the mechanical part, time-dependent Dirichlet and Neumann boundary conditions are defined by decomposing boundary surface $\partial\mathcal{B}_0 = \partial\mathcal{B}_0^{\varphi} \cup \partial\mathcal{B}_0^{t}$ with condition $\partial\mathcal{B}_0^{\varphi} \cap \partial\mathcal{B}_0^{t} = \emptyset$ as,

$$\boldsymbol{\varphi} = \bar{\boldsymbol{\varphi}}(\boldsymbol{X}, t) \text{ on } \partial\mathcal{B}_0^{\varphi} \quad \text{and} \quad \boldsymbol{\sigma} \cdot \boldsymbol{n} = \bar{\boldsymbol{t}}(\boldsymbol{x}, t) \text{ on } \partial\mathcal{B}_t^{\varphi} \tag{13}$$

with prescribed deformation $\bar{\boldsymbol{\varphi}}$ and the Eulerian traction vector $\bar{\boldsymbol{t}}$ along with its Lagrangian counterpart $\bar{\boldsymbol{T}} = J\bar{\boldsymbol{t}}$. Similarly, linear dependency of Hydrogen proton flux h on outward normal $\boldsymbol{n}$ through its spatial flux vector $\mathbb{h}$ in the current configuration is defined as

$$h(\boldsymbol{x}, t; \boldsymbol{n}) = \mathbb{h}(\boldsymbol{x}, t) \cdot \boldsymbol{n} \,. \tag{14}$$

H^+ flux in the reference configuration is defined as,

$$\mathbb{H}\, d\boldsymbol{A} = \mathbb{h}\, d\boldsymbol{a} \quad \text{with} \quad \mathbb{H} = \boldsymbol{F}^{-1}(J\mathbb{h}) \,. \tag{15}$$

Kirchhoff type H^+ flux can be defined as $\tilde{\mathbb{h}} = J\mathbb{h}$. On the other hand, linear dependency of the microforce traction ξ of chemical microforce $g(\boldsymbol{x}, t)$ on outward normal $\boldsymbol{n}$ is defined through spatial microforce traction vector $\mathbb{k}$ as,

$$\xi(\boldsymbol{x}, t; \boldsymbol{n}) = \mathbb{k}(\boldsymbol{x}, t) \cdot \boldsymbol{n} \,. \tag{16}$$

Material microforce traction $\mathbb{K}$ is defined as,

$$\mathbb{K}\, d\boldsymbol{A} = \mathbb{k}\, d\boldsymbol{a} \quad \text{with} \quad \mathbb{K} = \boldsymbol{F}^{-1}(J\mathbb{k}) \,. \tag{17}$$

Kirchhoff type microforce traction can be defined as $\tilde{\mathbb{k}} = J\mathbb{k}$. For the chemical part, time-dependent Dirichlet and Neumann boundary conditions are defined by decomposing boundary surface $\partial\mathcal{B}_0 = \partial\mathcal{B}_0^{c} \cup \partial\mathcal{B}_0^{\xi}$ and $\partial\mathcal{B}_0 = \partial\mathcal{B}_0^{\mu} \cup \partial\mathcal{B}_0^{h}$ with condition $\partial\mathcal{B}_0^{c} \cap \partial\mathcal{B}_0^{\xi} = \emptyset$ and $\partial\mathcal{B}_0^{\mu} \cap \partial\mathcal{B}_0^{h} = \emptyset$ as,

$$c = \bar{c}(\boldsymbol{X}, t) \text{ on } \partial\mathcal{B}_0^{c} \quad \text{and} \quad \mathbb{k}(\boldsymbol{x}, t) \cdot \boldsymbol{n} = \bar{\xi}(\boldsymbol{x}, t) \text{ on } \partial\mathcal{B}_t^{\xi} \,, \tag{18}$$

and

$$\mu = \bar{\mu}(\boldsymbol{X}, t) \text{ on } \partial\mathcal{B}_0^{\mu} \quad \text{and} \quad \mathbb{h}(\boldsymbol{x}, t) \cdot \boldsymbol{n} = \bar{h}(\boldsymbol{x}, t) \text{ on } \partial\mathcal{B}_t^{h} \,, \tag{19}$$

with prescribed concentration $\bar{c}$ and chemical potential $\bar{\mu}$. The Hydrogen proton flux $\bar{h}$ and its Lagrangian counterpart $\bar{H} = J\bar{h}$, the micro-traction $\bar{\xi}$ and its Lagrangian counterpart $\bar{\Xi} = J\bar{\xi}$, can as well be defined.

3.2. Phase-field method

For the phase-field problem, a sharp-crack surface topology $\Gamma \to \Gamma_l$ is regularized by the crack surface functional as outlined in Miehe et al. [56]

$$\Gamma_l(d) = \int_{\mathcal{B}_0} \gamma_l(d, \nabla d)\, dV \quad \text{with} \quad \gamma_l(d, \nabla d) = \frac{1}{2l_s}d^2 + \frac{l_s}{2}\|\nabla d\|^2 \,, \tag{20}$$

based on the crack surface density function γ_l per unit volume of the solid and the fracture length scale parameter l_s that governs the regularization. To describe a purely geometric approach to phase-field fracture, the regularized crack phase-field d is obtained by a minimization principle of diffusive crack topology

$$d = \text{Arg}\,\{\inf_{d} \Gamma_l(d)\} \quad \text{with} \quad d = 1 \text{ on } \Gamma \subset \mathcal{B}_0 \tag{21}$$

as Dirichlet boundary condition for the given crack surface topology. This yields Euler equation $d - l_s^2 \Delta d = 0$ in $\mathcal{B}_0$. Evolution of the regularized crack surface functional (20) can be driven by the constitutive functions as outlined in [3], postulating a global evolution equation of regularized crack surface as

$$\frac{d}{dt}\Gamma_l(d) =:= \frac{1}{l_s}\int_{\mathcal{B}_0} [\ (1-d)\mathcal{H} - \eta\dot{d}\ ]\cdot\dot{d}\, dV \geq 0\ , \tag{22}$$

where $\eta \geq 0$ is a parameter that characterizes the artificial/numerical viscosity of the crack propagation. The term $\eta\dot{d}$ represents the viscous crack resistance and $(1-d)\mathcal{H}$ is a crack driving force. The effective crack driving force

$$\mathcal{H} = \max_{\mathfrak{s}\in[0,t]} D(\boldsymbol{x},\mathfrak{s}) = \max \frac{2\psi^{e+}}{G_c/l_s} \geq 0\ , \tag{23}$$

is introduced as the local history variable in the full process history $\mathfrak{s} \in [0,t]$. $\mathcal{H}$ accounts for the irreversibility of the phase-field evolution by filtering out a maximum value of what is known as the crack driving state function D.

3.3. Electrochemical surface reaction kinetics

Electrochemical reaction kinetics determines the spatial Hydrogen proton flux which represents the splitting/evolution reactions of H^+. Thus it is modelled by using the Butler-Volmer equation. This reaction gives the current density i at a point on the surface in terms of surface overpotential η_s. Surface overpotential is calculated as the difference between the applied potential V and open circuit potential U_{ocp}. Local current density i is calculated according to the Butler-Volmer equation as,

$$i = i_0\left(\exp\left[\frac{\beta F\,\eta_s}{R\,\theta}\right] - \exp\left[-\frac{(1-\beta)\,F\,\eta_s}{R\,\theta}\right]\right). \tag{24}$$

Here, i_0 is the exchange current density, β is the symmetry factor, R is the gas constant and θ is the temperature in Kelvin. The exchange current density i_0 is computed as

$$i_0 = F\,k\,c_{max}\,(1-c)^{1-\beta}\,c^{\beta}\,c_{amb}^{1-\beta} \tag{25}$$

where k is the reaction rate and $c_{amb} \in [0,1]$ is the dimensionless H^+ concentration in the surrounding bulk. Faraday's law relates the movement of proton mass m to the current density i as

$$m = \frac{m_{mol}\,i\,A\,t}{z\,F}\ . \tag{26}$$

Here, m_{mol} is the molecular weight, $z = 1$ is the valence of a Hydrogen proton, A is the surface area and t is the time. H^+ flux density computed by taking a time derivative of Faraday's law is

$$\hat{h} = \frac{1}{A\,m_{mol}}\frac{d}{dt}m = \frac{i}{F}\ . \tag{27}$$

From the above equation, the net H^+ flux density is calculated as

$$h := \hat{h}/c_{max} = \frac{i_0}{F\,c_{max}}\left(\exp\left[\frac{\beta F\,\eta_s}{R\,\theta}\right] - \exp\left[-\frac{(1-\beta)\,F\,\eta_s}{R\,\theta}\right]\right). \tag{28}$$

Here, flux density can be decomposed into a function of H^+ concentration and a function of surface voltage as

$$h = h_1(c)\cdot h_2(\eta_s)\ . \tag{29}$$

As a function of chemical concentration, h_1 is written as,

$$h_1(c) := \frac{i_0}{F\,c_{max}} = k\,\{c_{amb}\,(1-c)\}^{1-\beta}c^{\beta}\ , \tag{30}$$

where, k is net reaction rate. Also, h_2 as a function of surface voltage η_s is given by

$$h_2(\eta_s) := \left(\exp\left[\frac{\beta\, F\, \eta_s}{R\,\theta}\right] - \exp\left[-\frac{(1-\beta)\, F\, \eta_s}{R\,\theta}\right]\right). \tag{31}$$

It should be noted that decoupling of Hydrogen flux will simplify the implementation of the Hydrogen flux through elements of the catalyst layer. Electrochemical reaction kinetics at free cracked surfaces is assumed identical to the chemical flux formation from PTL/CL interface according to [54]. This is modeled by an additional source term in the balance of H^+ mass. The electrochemical reaction kinetics on the cracked surfaces $\gamma^{\pm}$ is assumed identical to the aforementioned chemical flux as,

$$h^{\pm}(c^{\pm}) = h_1(c^{\pm})\; h_2(\eta_s)\,. \tag{32}$$

Herein, $c^{\pm}$ are the concentrations at the crack surfaces $\gamma^{\pm}$. Therefore, the total influx through the crack surfaces

$$S = -\int_{\Gamma}(h^{+} + h^{-})dA = -\int_{\Gamma}[h_1(c^{+}) + h_1(c^{-})]\; h_2(\eta_s)\; dA = -\int_{\Gamma} 2\; h_1(c)\; h_2(\eta_s)\; dA \tag{33}$$

is assumed to be integral over the area dA. Now, the phase-field fracture approach can be implemented by using regularization of a surface element $dA \approx \gamma_l(d;\nabla d)dV$ and it results into

$$S \approx S_l = -\int_{\mathcal{B}_0} 2\; h_1(c)\; h_2(\eta_s)\gamma_l(d;\nabla d)\; dV\,. \tag{34}$$

The addition of the source term into the chemical balance equation with spatial regularization can be assumed with damage profile $d(x) = \exp[-|x|/l_s]$ as

$$s = -2h_1(c)\; h_2(\eta_s)\frac{1}{2l_s}[d^2 + l_s^2|\nabla d|^2]\,. \tag{35}$$

In line with work [54], d^2 term will induce a quadratic increase of electrochemical action on the crack face which formulates the source term as

$$s = -\frac{2}{l_s}\; h_1(c)\; h_2(\eta_s)d^2\,. \tag{36}$$

3.4. Objective free energy storage function for bulk response

The free energy can be considered as a function of primary variables from equation 6 and their gradients such as

$$\psi = \tilde{\psi}(\boldsymbol{\varphi}, \nabla\boldsymbol{\varphi}, c, \nabla c; d)\,. \tag{37}$$

A reduced form of free energy function can be obtained by applying invariance of $\tilde{\psi}$ with respect to the rigid body motion superimposed on current configuration for all translations and rotation as,

$$\psi = \widehat{\psi}(\boldsymbol{F}, c, \mathbb{C}; d) = \widehat{\psi}(\boldsymbol{C}, c, \mathbb{C}; d)\,. \tag{38}$$

Here, $\boldsymbol{F}$ is the deformation gradient, $\boldsymbol{C}$ is the right Cauchy-Green tensor and $\mathbb{C}$ is the gradient of the chemical concentration. The free energy storage function decomposes into elastic and chemical contributions and contains additionally an interface term, consistent with the classical Cahn-Hilliard theory,

$$\widehat{\psi}(\boldsymbol{F}, c, \mathbb{C}) = (1-d)^2\psi_{mec}(\boldsymbol{F}, c) + \psi_{che}(c) + \psi_{int}(\mathbb{C})\,. \tag{39}$$

3.4.1. Mechanical free energy

In order to describe the mechanical free energy, we first multiplicatively split the deformation gradient into mechanical and chemical parts

$$\boldsymbol{F} = \boldsymbol{F}_e\boldsymbol{F}_c \quad \text{where} \quad \boldsymbol{F}_e = J_c^{-1/3}\boldsymbol{F}, \quad \text{and} \quad J_c = \det \boldsymbol{F}_c = 1 + \Omega(c - c_0)\,. \tag{40}$$

The mechanical part $\boldsymbol{F}_e$ of the deformation gradient is responsible for elastic reversible deformations whereas the chemical part $\boldsymbol{F}_c := J_c^{1/3}\mathbf{1}$ is responsible for isotropic swelling due the change of Hydrogen proton concentration. Herein, J_c is the volumetric swelling. The mechanical part or the elastic contribution to the free energy is assumed to have a compressible neo-Hookean form,

$$\psi_{mec}(\boldsymbol{F}_e) = \frac{\lambda}{2}(\ln J^e)^2 + \frac{\hat{\mu}}{2}(I_1^e - 2\ln J^e - 3) \tag{41}$$

with

$$I_1^e = \mathrm{tr}[\boldsymbol{F}_e{}^T \boldsymbol{F}_e] \quad \text{and} \quad J^e = \det \boldsymbol{F}_e \,, \tag{42}$$

where the parameters λ and $\hat{\mu}$ are the first Lamé constant and shear modulus, respectively.

3.4.2. Chemical free energy

The Cahn-Hilliard type chemical free energy

$$\psi_{che}(c) = A[c\ln c + (1-c)\ln(1-c)] + Bc(1-c) \tag{43}$$

describes a double well potential function that accounts for the phase separation. The first term, governed by the parameter A, ensures that the concentration remains in the range $c \in [0,1]$ while the second term, governed by the parameter B, ensures a non-convex domain $B > 2A$ for two distinct phases, see also [12; 26; 54].

3.4.3. Interfacial free energy

From Cahn-Hilliard chemical free energy for the biphasic mixture ($B > 0$), one can determine the volume of individual chemical phase by using a common tangent method followed by simple algebraic calculations. But this volume calculation of the individual chemical species phase does not address the size or number of phase particles. It can either be a few large particles or many small particles, however, the interface area would be different for both cases even if the total volume is the same. Hence, the interface free energy must be calculated when there is phase separation otherwise it will result in the mathematically ill-posed or physically wrong formulation. In biphasic mixtures, the jump in the concentration along the interface cannot be ignored. In this regard, a quadratic free energy function

$$\psi_{int}(\mathbb{C}) = \frac{C}{2}\,|\mathbb{C}^2| \quad \text{where} \quad \mathbb{C} = \nabla c \tag{44}$$

is the concentration gradient is adopted. Herein, the gradient parameter C that acts as a penalty term that smears out sharp concentration gradients.

3.5. Dissipation function

The H^+ is prescribed by using objective dissipation potential ϕ. It is assumed that the specimen flux dissipation potential has a convex quadratic form

$$\phi = \widehat{\phi}(\mathbb{M}; \boldsymbol{F}, c, d, \boldsymbol{X}) = \frac{c(1-c)}{2}\widehat{M}(d)\Big[\boldsymbol{C}^{-1} : (\mathbb{M}\otimes\mathbb{M})\Big] \tag{45}$$

and depends on the negative gradient $\mathbb{M} := -\nabla\mu$ of the chemical potential. This form is related to the Cauchy-Green tensor $\boldsymbol{C} = \boldsymbol{F}^T\boldsymbol{F}$ and concentration c that defines the given chemo-mechanical state. Here, the Hydrogen proton mobility is described by the function $\widehat{M} \geq 0$ that degrades with a fracture in the following way

$$\widehat{M}(d) = (1-d)^2 M \tag{46}$$

multiplication of the phase-field d with H^+ mobility $M \geq 0$ describes the coupling between diffusion and fracture. The mobility of the Hydrogen protons are assumed to vanish for a fully developed crack.

3.6. Constitutive equations

The CCM solid skeleton has to satisfy the equation of equilibrium, representing the first partial differential equation PDE for the coupled problem as

$$\boxed{\text{Div}[\boldsymbol{P}] + \overline{\boldsymbol{\gamma}} = 0} \tag{47}$$

where dynamic effects are neglected and $\overline{\boldsymbol{\gamma}}$ is a given body force field per unit volume of the reference configuration. From the energetic response function (39) it is possible to derive the constitutive first Piola-Kirchhoff stress as

$$\boldsymbol{P} = \partial_{\boldsymbol{F}}\widehat{\psi}(\boldsymbol{F}, c, \mathbb{C}; d, \boldsymbol{X}) = (1-d)^2 J_c^{-1/3}[\lambda \ln J^e \boldsymbol{F}_e^{-T} + \hat{\mu}(\boldsymbol{F}_e - \boldsymbol{F}_e^{-T})] \,. \tag{48}$$

The Hydrogen proton in the CL bulk has to satisfy the balance of mass (conservation of species), reflecting the second PDE for the coupled problem as

$$\boxed{\dot{c} + \text{Div}[\mathbb{H}] - s = 0} \tag{49}$$

where s is the source term defined in (36) and the constitutive Hydrogen proton flux is obtained from the dissipation potential in (45) by

$$\mathbb{H} = \partial_{\mathbb{M}}\widehat{\phi}(\mathbb{M}; \boldsymbol{F}, c, d, \boldsymbol{X}) = c(1-c)[(1-d)^2 \boldsymbol{M}]\boldsymbol{C}^{-1}\mathbb{M} \,. \tag{50}$$

The third PDF is the balance of chemical micro-forces, defined as

$$\boxed{g + \text{Div}[\mathbb{K}] = 0} \tag{51}$$

with

$$g = \mu - \partial_c\widehat{\psi}(\boldsymbol{F}, c, \mathbb{C}; d, \boldsymbol{X}) \quad \text{and} \quad \mathbb{K} = \partial_{\mathbb{C}}\widehat{\psi}(\boldsymbol{F}, c, \mathbb{C}; d, \boldsymbol{X}) \tag{52}$$

where the the chemical potential μ and the micro-traction are obtained from the energy in (39) by

$$\mu = A \ln[\frac{c}{1-c}] + B(1-2c) + \Omega J_c^{-1} p \quad \text{and} \quad \mathbb{K} = C\nabla c \,. \tag{53}$$

Here, pressure field p is defined as $p = -\frac{1}{3}tr[\tilde{\boldsymbol{\sigma}}]$. The fourth PDF of the coupled problem is the crack phase-field evolution in the domain $\mathcal{B}_0$ along with its homogeneous Neumann boundary condition as

$$\boxed{[\, d - l_s^2 \Delta d \,] + \eta\dot{d} + (d-1)\mathcal{H} = 0} \tag{54}$$

with $\nabla d \cdot \boldsymbol{n} = 0$ on $\partial\mathcal{B}_0$. In this equation, first term represents geometric resistance, second term term represents crack evolution and the third term is the driving force.

In all balance equations, spatial divergence terms are converted to material divergence terms in reference configuration by using Jacobian relations as $\text{Div}[\boldsymbol{P}] = J\ \text{Div}_x[\boldsymbol{\sigma}]$, $\text{Div}[\mathbb{H}] = J\ \text{Div}_x[\mathbb{h}]$ and $\text{Div}[\mathbb{K}] = J\ \text{Div}[\mathbb{k}]$. Furthermore, all material terms can be converted into spatial terms by using the stress relations as $\boldsymbol{P} = (J\boldsymbol{\sigma})\boldsymbol{F}^{-T}$, material flux $\mathbb{H} = \boldsymbol{F}^{-1}(J\mathbb{h})$ and material chemical microforce traction $\mathbb{K} = \boldsymbol{F}^{-1}(J\mathbb{k})$.

3.7. Time discretization scheme

A finite time increment $\Delta t = t_{n+1} - t_n$ denoting the time step is considered. All state variables at time step t_n are assumed to be known and at time step t_{n+1} are to be computed. The time-dependent chemical concentration of Hydrogen ions is given by governing partial differential equation as

$$\frac{c - c_n}{\Delta t} + \text{Div}[\mathbb{H}] - s = 0 \,. \tag{55}$$

Therein, the backward Euler scheme is used for all variables. In the sequel, the same scheme is adopted for all local time derivatives appearing in each sub-problem.

4. Weak formulations and FEM implementation of the coupled problem

4.1. Weak form of the bulk response equations in Lagrange configuration

The bulk response of the system, which consists of the chemical concentration, chemical potential and displacement as the primary variables is presented in Lagrangian configuration as follows.

$$\begin{aligned}
G_\varphi(\boldsymbol{\varphi}, c, \mu, d; \delta\boldsymbol{\varphi}) &= \int_{\mathcal{B}_0} [\boldsymbol{P} : \nabla\delta\boldsymbol{\varphi} - \boldsymbol{\gamma}\cdot\delta\boldsymbol{\varphi}]\, dV - \int_{\partial\mathcal{B}_t^t} \bar{\boldsymbol{T}}\cdot\delta\boldsymbol{\varphi}\, dA = 0\,,\\
G_\mu(\boldsymbol{\varphi}, c, \mu, d; \delta\mu) &= \int_{\mathcal{B}_0} \left[\mathbb{H}\cdot\nabla\delta\mu - \left(\frac{c-c_n}{\Delta t} - s\right)\delta\mu\right] dV - \int_{\partial\mathcal{B}_t^h} \bar{H}\cdot\delta\mu\, dA = 0\,,\\
G_c(\boldsymbol{\varphi}, c, \mu, d; \delta c) &= \int_{\mathcal{B}_0} [\mathbb{K}\cdot\nabla\delta c - g\delta c]\, dV - \int_{\partial\mathcal{B}_t^\xi} \bar{\Xi}\cdot\delta c\, dA = 0\,,\\
G_d(\boldsymbol{\varphi}, c, \mu, d; \delta d) &= \int_{\mathcal{B}_0} \left[\left(\eta\,\frac{d-d_n}{\Delta t} + d - (1-d)\mathcal{H}\right)\delta d + \nabla d\cdot l_s^2\nabla\delta d\right] dV = 0\,.
\end{aligned} \tag{56}$$

4.2. Weak form of the bulk response equations in Eulerian configuration

The eulerian setting is generally preferred because of the sparse B matrix which makes the computations faster [101]. Weak form of bulk response equations in the Eulerian setting can be written with the help of $\boldsymbol{\sigma}$, $\mathbb{h}$, $\mathbb{k}$ and $dv = JdV$ as,

$$\begin{aligned}
g_\varphi(\boldsymbol{\varphi}, c, \mu, d; \delta\boldsymbol{\varphi}) &= \int_{\mathcal{B}_t} [\boldsymbol{\sigma} : \nabla_x\delta\boldsymbol{\varphi} - \boldsymbol{\gamma}\cdot\delta\boldsymbol{\varphi}]\, dv - \int_{\partial\mathcal{B}_t^t} \bar{\boldsymbol{t}}\cdot\delta\boldsymbol{\varphi}\, da = 0\,,\\
g_\mu(\boldsymbol{\varphi}, c, \mu, d; \delta\mu) &= \int_{\mathcal{B}_t} \left[\mathbb{h}\cdot\nabla_x\delta\mu - \left(\frac{c-c_n}{\Delta t} - s\right)\delta\mu\right] dv - \int_{\partial\mathcal{B}_t^h} \bar{h}\cdot\delta\mu\, da = 0\,,\\
g_c(\boldsymbol{\varphi}, c, \mu, d; \delta c) &= \int_{\mathcal{B}_t} [\mathbb{k}\cdot\nabla_x\delta c - g\delta c]\, dv - \int_{\partial\mathcal{B}_t^\xi} \bar{\xi}\cdot\delta c\, da = 0\,,\\
g_d(\boldsymbol{\varphi}, c, \mu, d; \delta d) &= \int_{\mathcal{B}_0} \left[\left(\eta\,\frac{d-d_n}{\Delta t} + d - (1-d)\mathcal{H}\right)\delta d + \nabla_x d\cdot l_s^2\nabla_x\delta d\right] dv = 0\,.
\end{aligned} \tag{57}$$

4.3. Finite element discretisation

Considering the standard finite element discretisation of the spatial domain of the initial configuration $\mathcal{B}_0$ and Neumann surfaces of the current configuration $\mathcal{B}_t$, one can write

$$\mathcal{B}_0 = \bigcup_{e=1}^{N_e} \mathcal{B}_0^e\,,\quad \partial\mathcal{B}_t^t = \bigcup_{s^t=1}^{N_s^t} \partial\mathcal{B}_t^{t\ s^t}\,,\quad \partial\mathcal{B}_t^h = \bigcup_{s^h=1}^{N_s^h} \partial\mathcal{B}_t^{h\ s^h}\,,\quad \partial\mathcal{B}_t^\xi = \bigcup_{s^h=1}^{N_s^\xi} \partial\mathcal{B}_t^{\xi\ s^h}\,. \tag{58}$$

In the above equations, N_e is the number of bulk elements, N_s^t is the number of the surface elements for traction, N_s^h is the number of surface elements for the H^+ flow and N_s^ξ is the number of surface elements microforce. The discretization is based on finite element shape functions and their respective derivatives with respect to reference and spatial geometries read

$$\begin{aligned}
&\boldsymbol{\varphi}(\boldsymbol{x}) = \boldsymbol{N}_\varphi^s(\boldsymbol{x})\,\boldsymbol{d}_\varphi\,, && \nabla\boldsymbol{\varphi}(\boldsymbol{x}) = \bar{\boldsymbol{B}}_\varphi^s(\boldsymbol{x})\,\boldsymbol{d}_\varphi\,, && \nabla_x\boldsymbol{\varphi}(\boldsymbol{x}) = \boldsymbol{B}_\varphi^s(\boldsymbol{x})\,\boldsymbol{d}_\varphi\\
&c(\boldsymbol{x}) = \boldsymbol{N}_c^s(\boldsymbol{x})\,\boldsymbol{d}_c\,, && \nabla c(\boldsymbol{x}) = \bar{\boldsymbol{B}}_c^s(\boldsymbol{x})\,\boldsymbol{d}_c\,, && \nabla_x c(\boldsymbol{x}) = \boldsymbol{B}_c^s(\boldsymbol{x})\,\boldsymbol{d}_c\\
&\mu(\boldsymbol{x}) = \boldsymbol{N}_\mu^s(\boldsymbol{x})\,\boldsymbol{d}_\mu\,, && \nabla\mu(\boldsymbol{x}) = \bar{\boldsymbol{B}}_\mu^s(\boldsymbol{x})\,\boldsymbol{d}_\mu\,, && \nabla_x\mu(\boldsymbol{x}) = \boldsymbol{B}_\mu^s(\boldsymbol{x})\,\boldsymbol{d}_\mu\\
&d(\boldsymbol{x}) = \boldsymbol{N}_d^s(\boldsymbol{x})\,\boldsymbol{d}_d\,, && \nabla d(\boldsymbol{x}) = \bar{\boldsymbol{B}}_d^s(\boldsymbol{x})\,\boldsymbol{d}_d\,, && \nabla_x d(\boldsymbol{x}) = \boldsymbol{B}_d^s(\boldsymbol{x})\,\boldsymbol{d}_d\,.
\end{aligned} \tag{59}$$

Here, $\boldsymbol{N}$ and $\bar{\boldsymbol{B}}$ and $\boldsymbol{B}$ are the shape functions and their derivatives with respect to reference and spatial configurations, respectively. Hence, by using given finite element discretization, the residuum in the current configuration $\mathcal{B}$ can be written as,

$$
\begin{aligned}
\boldsymbol{R}_\varphi(\boldsymbol{d}_\varphi, \boldsymbol{d}_c, \boldsymbol{d}_\mu, \boldsymbol{d}_d) &= \mathop{\mathsf{A}}_{e=1}^{N_e} \int_{\mathcal{B}^e} [\boldsymbol{B}_\varphi^{eT} \boldsymbol{\sigma} - \boldsymbol{N}_\varphi^{eT} \bar{\boldsymbol{\gamma}}]\, dv - \mathop{\mathsf{A}}_{s^t=1}^{N_s^t} \int_{\partial\mathcal{B}^{s^t}} \boldsymbol{N}_\varphi^{sT} \bar{\boldsymbol{t}}\, da = 0\,, \\
\boldsymbol{R}_c(\boldsymbol{d}_\varphi, \boldsymbol{d}_c, \boldsymbol{d}_\mu, \boldsymbol{d}_d) &= \mathop{\mathsf{A}}_{e=1}^{N_e} \int_{\mathcal{B}^e} \left[\boldsymbol{B}_\mu^{eT} \mathbb{h} - \boldsymbol{N}_\mu^{eT} \left(\frac{c - c_n}{\Delta t} - s\right)\right] dv - \mathop{\mathsf{A}}_{s^h=1}^{N_s^h} \int_{\partial\mathcal{B}^{h s^h}} \boldsymbol{N}_\mu^{s^T} \bar{h}\, da = 0\,, \\
\boldsymbol{R}_\mu(\boldsymbol{d}_\varphi, \boldsymbol{d}_c, \boldsymbol{d}_\mu, \boldsymbol{d}_d) &= \mathop{\mathsf{A}}_{e=1}^{N_e} \int_{\mathcal{B}^e} [\boldsymbol{B}_c^{eT} \mathbb{k} - \boldsymbol{N}_c^{eT} g]\, dv - \mathop{\mathsf{A}}_{s^h=1}^{N_s^h} \int_{\partial\mathcal{B}^{\xi s^h}} \boldsymbol{N}_c^{sT} \bar{h}\, da = 0\,, \\
\boldsymbol{R}_d(\boldsymbol{d}_\varphi, \boldsymbol{d}_c, \boldsymbol{d}_\mu, \boldsymbol{d}_d) &= \mathop{\mathsf{A}}_{e=1}^{N_e} \int_{\mathcal{B}^e} \left[\boldsymbol{N}_d^{eT} \left(\eta\, \frac{d - d_n}{\Delta t} + d - (1 - d)\mathcal{H}\right) + \bar{\boldsymbol{B}}_d^{eT} l_s^2 \nabla d\right] dV = 0\,.
\end{aligned}
\tag{60}
$$

4.4. Solution of the algebraic coupled problem

The nonlinear system of equations for the bulk response given in 60 are solved using Newton-Raphson iterations. The system of equations can be written in simplified notations as

$$
\boldsymbol{R} = [\boldsymbol{R}_\varphi\ \boldsymbol{R}_c\ \boldsymbol{R}_\mu\ \boldsymbol{R}_d]^T \quad \text{and} \quad \boldsymbol{d} = [\boldsymbol{d}_\varphi\ \boldsymbol{d}_c\ \boldsymbol{d}_\mu\ \boldsymbol{d}_d]^T\,. \tag{61}
$$

Hence, the electro-chemo-mechanical bulk response can be solved by using

$$
\boldsymbol{R}(\boldsymbol{d}) = 0\,. \tag{62}
$$

Therefore, the Newton-Raphson scheme is used for solving the above-mentioned problem by using updates as

$$
\boldsymbol{d}^{k+1} \leftarrow \boldsymbol{d}^k - [D\boldsymbol{R}(\boldsymbol{d})]^{-1}\, \boldsymbol{R}^k\,. \tag{63}
$$

Table 1: Operator-splitting algorithm based on sequential update for the multi-field problem in $[t_n, t_{n+1}]$

Given: The generalized displacement field $\boldsymbol{d} = [\boldsymbol{d}_\varphi^n, \boldsymbol{d}_\mu^n, \boldsymbol{d}_c^n, \boldsymbol{d}_d^n]^T$ from $t = t_n$.
Initialization: $k = 0$; Set $\boldsymbol{d}^k \leftarrow \boldsymbol{d}^n$

1. Solve and update each sub-step

$$
\begin{aligned}
&\textsc{Algo}_{\textsc{M}}: \quad \textsc{Solve} \quad \boldsymbol{K}_{\varphi\varphi} \Delta\boldsymbol{d}_\varphi = -\boldsymbol{R}_\varphi \\
&\textsc{Algo}_{\textsc{M}}: \quad \textsc{Update} \quad \boldsymbol{d}_\varphi^{k+1} = \boldsymbol{d}_\varphi^k + \Delta\boldsymbol{d}_\varphi \qquad \textsc{while} \quad |\boldsymbol{R}_\varphi| \geq \textsc{Tol} \\
&\textsc{Algo}_{\textsc{C}}: \quad \textsc{Solve} \quad \begin{bmatrix} \boldsymbol{K}_{\mu\mu} & \boldsymbol{K}_{\mu c} \\ \boldsymbol{K}_{c\mu} & \boldsymbol{K}_{cc} \end{bmatrix} \begin{bmatrix} \Delta\boldsymbol{d}_\mu \\ \Delta\boldsymbol{d}_c \end{bmatrix} = - \begin{bmatrix} \boldsymbol{R}_\mu \\ \boldsymbol{R}_c \end{bmatrix} \\
&\textsc{Algo}_{\textsc{C}}: \quad \textsc{Update} \quad \begin{bmatrix} \boldsymbol{d}_\mu^{k+1} \\ \boldsymbol{d}_c^{k+1} \end{bmatrix} = \begin{bmatrix} \boldsymbol{d}_\mu^k \\ \boldsymbol{d}_c^k \end{bmatrix} + \begin{bmatrix} \Delta\boldsymbol{d}_\mu \\ \Delta\boldsymbol{d}_c \end{bmatrix} \qquad \textsc{while} \quad \left| \begin{matrix} \boldsymbol{R}_\mu \\ \boldsymbol{R}_c \end{matrix} \right| \geq \textsc{Tol} \\
&\textsc{Algo}_{\textsc{D}}: \quad \textsc{Solve} \quad \boldsymbol{K}_{dd} \Delta\boldsymbol{d}_d = -\boldsymbol{R}_d \\
&\textsc{Algo}_{\textsc{D}}: \quad \textsc{Update} \quad \boldsymbol{d}_d^{k+1} = \boldsymbol{d}_d^k + \Delta\boldsymbol{d}_d \qquad \textsc{while} \quad |\boldsymbol{R}_d| \geq \textsc{Tol}
\end{aligned}
$$

2. Update $k \leftarrow k + 1$

Table 1: Material parameters used in the numerical examples.

No.	Parameter name	Parameter	Value	Unit
1.	Lame's constant	λ	57.69	N mm^{-2}
2.	Shear modulus	$\hat{\mu}$	38.46	N mm^{-2}
3.	Young's modulus	E	100	N mm^{-2}
4.	Poisson's ratio	ν	0.3	-
5.	Griffith's fracture energy	G_c	0.001	N mm^{-1}
6.	Fracture viscosity	η	10^{-6}	-
7.	Universal gas constant	R	8.3145	J mol^{-1} K^{-1}
8.	Faraday's constant	F	96485	Coulumb mol^{-1}
9.	Symmetry factor	β	0.5	-
10.	Swelling parameter	Ω	1.1	-
11.	Chemical energy parameter	A	56.98	N mm^{-2}
12.	Phase separation parameter	B	0	N mm^{-2}
13.	Interface energy parameter	C	0	N mm^{-4}
14.	Initial concentration	c_0	0.1	-
15.	Diffusion parameter	M	10^{-5}	mm^4 N^{-1} s^{-1}
16.	Surface coefficient	h_0	10^{-6}	mm s^{-1}
17.	Time step	Δt	10^{-2}	s

Convergence of the nonlinear system is achieved when $\|\boldsymbol{R}\| < \text{TOL}$. Here, $D[\boldsymbol{R}(\boldsymbol{d})]$ is a full linearization of the system and computed as a monolithic tangent, for details of tangent matrix computation and assembly. We adopt an single-pass sequential update algorithm based on operator-splitting

$$\text{ALGO} = \text{ALGO}_{\text{D}} \circ \text{ALGO}_{\text{C}} \circ \text{ALGO}_{\text{M}} \,, \tag{64}$$

that solves the mechanical, chemical Cahn-Hilliard type diffusion, and the crack phase-field parts, respectively. Each sub-algorithm perform, repectively, the following upadates

$$\begin{aligned}
&\text{ALGO}_{\text{M}} : \quad \text{SOLVE} \quad \boldsymbol{K}_{\varphi\varphi}\Delta\boldsymbol{d}_{\varphi} = -\boldsymbol{R}_{\varphi} \quad \longrightarrow \quad \text{UPDATE} \quad \boldsymbol{d}_{\varphi}^{k+1} = \boldsymbol{d}_{\varphi}^{k} + \Delta\boldsymbol{d}_{\varphi} \\
&\text{ALGO}_{\text{C}} : \quad \text{SOLVE} \quad \begin{bmatrix} \boldsymbol{K}_{\mu\mu} & \boldsymbol{K}_{\mu c} \\ \boldsymbol{K}_{c\mu} & \boldsymbol{K}_{cc} \end{bmatrix} \begin{bmatrix} \Delta\boldsymbol{d}_{\mu} \\ \Delta\boldsymbol{d}_{c} \end{bmatrix} = - \begin{bmatrix} \boldsymbol{R}_{\mu} \\ \boldsymbol{R}_{c} \end{bmatrix} \quad \longrightarrow \quad \text{UPDATE} \quad \begin{bmatrix} \boldsymbol{d}_{\mu}^{k+1} \\ \boldsymbol{d}_{c}^{k+1} \end{bmatrix} = \begin{bmatrix} \boldsymbol{d}_{\mu}^{k} \\ \boldsymbol{d}_{c}^{k} \end{bmatrix} + \begin{bmatrix} \Delta\boldsymbol{d}_{\mu} \\ \Delta\boldsymbol{d}_{c} \end{bmatrix} \\
&\text{ALGO}_{\text{D}} : \quad \text{SOLVE} \quad \boldsymbol{K}_{dd}\Delta\boldsymbol{d}_{d} = -\boldsymbol{R}_{d} \quad \longrightarrow \quad \text{UPDATE} \quad \boldsymbol{d}_{d}^{k+1} = \boldsymbol{d}_{d}^{k} + \Delta\boldsymbol{d}_{d}
\end{aligned} \tag{65}$$

Herein, $\boldsymbol{K}_{ij}$ for $i, j = \{\varphi, \mu, c, d\}$ are tangent matrices for mechanical part, Cahn-Hilliard type diffusion, and crack phase-field parts, respectively.

5. Representative numerical examples

This section demonstrates the performance of the proposed phase-field model for electro-chemo-mechanically induced fracture in the anode and cathode catalyst layers in (CCM). The material parameters used in both boundary value problems (BVPs) are mentioned in table 1. As stated in the developed algorithm in section 4.4, we solve the coupled problem by using an alternate minimization scheme by using a nested Newton-Raphson algorithm. We first solve for d by fixing (u, c, μ) and then solving for the monolithic bulk response (u, c, μ) by fixing the updated d. Since all formulations are linearized in a consistent manner, quadratic convergence is achieved within a load step.

5.1. Experimentally inspired BVPs setup

In this contribution, we propose two numerical examples representing the experimentally observed coupled problem in PEMWE cells.

- It is known that at the anode-side, feed water from PTL will be split into Hydrogen proton and hydroxyl radical. Oxygen will form bubbles and released at the anode chamber. Whereas, Hydrogen proton will diffuse inside the CCM and travel towards the cathode electrode. During this process CCM experience huge deformations and cracking due to the coupled electro-chemo-mechanical processes. In the first boundary value problem, this phenomena has been formulated and proven numerically.
- After traveling of Hydrogen proton towards the cathode-side, CL will be saturated with Hydrogen protons. Due to the Hydrogen evolution reaction in the catalyst, bubbles of Hydrogen gas will be formed and released through cracks, as observed experimentally in [92; 93]. In the second boundary value problem, we mimic this behaviour for cathode catalyst at the size of one agglomerate particle. For the sake of simplicity, only Hydrogen proton transport mechanism is considered and the phase change is neglected. Herein, the catalyst agglomerate depicts a representative volume element (RVE) from the initially mechanically stressed catalyst layer and saturated with Hydrogen proton, inspired from [73; 74; 2; 104].

5.2. BVP1: Fracture of a simplified CL layer in anodic half cell

As a first benchmark test, we simulate the fracture induced in a simplified CCM structure due to electro-chemo-mechanical process at the PTL/CL interface. The key goal of this investigation is to gain the first insight about the

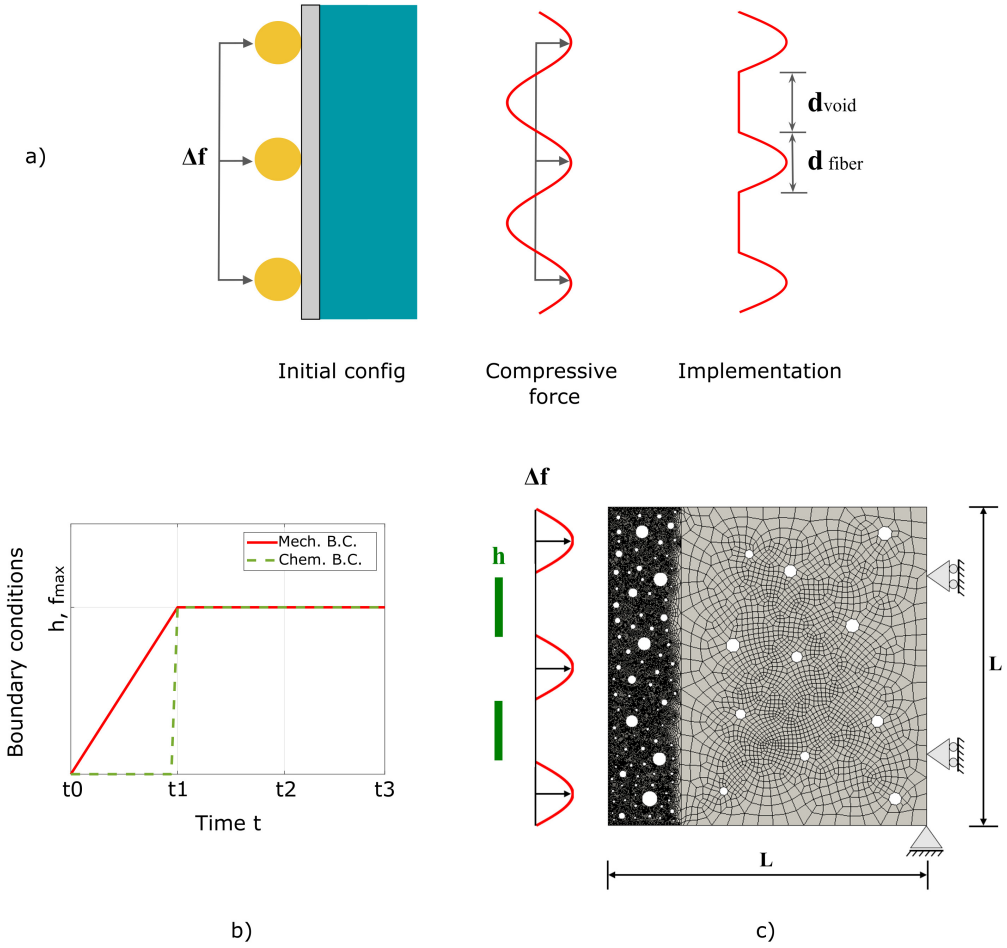

Figure 5: Boundary value problem setup. a) Implementation of the sinusoidal half wave force multiplier for PTL/CCM interaction with given fiber diameter and pore space; b) implementation of different boundary conditions with respect to time; and c) geometry and boundary conditions for simulation on CCM with Hydrogen proton flux at the interface.

qualitative illustration of the effects of externally applied force on CCM and Hydrogen diffusion on catalyst failure at the microscopic length scale. In this study, we have considered the cell setup procedure, inspired from [45; 78; 80], in order to formulate the boundary value problem. Hereby the effects of dry compression along with the electro-chemical process are investigated.

Assembly of the PEMWE cell components is according to the arrangement as illustrated in figure 4 (left). Thereafter, mechanical pressure is applied externally from both sides. Next, the cell operation is started with the deionized feed water and potentiostatic voltage supply. Operating PEMWE cell along with the deformed CL due to compression and Hydrogen proton influx at PTL/CL interface can be schematically visualised in figure 4 (right). As discussed in Section 2.4, modeling assumptions for this boundary value problem includes diffusion of the only protons through the CCM. Hydrogen proton influx within CL is modeled with the Butler-Volmer reaction kinetics. Incorporation of additional influx of the Hydrogen proton through the developing cracks at the CL is done automatically via the source term as described in Section 3.3.

We propose a boundary value problem (BVP) at the microscale considering the cell setup procedure, as shown in figure 5. Following [17] investigations, PTL surface morphology (i.e. pore and particle size), determines the level of CCM deformation and extent of losses associated with the proton transport in anode catalyst layer. Hence, a simple method for mimicking PTL morphology on PTL/CCM interface is developed. In this problem, we have considered contact between three PTL fibers with anode catalyst and membrane. Compressing the PTL fiber on the CL gives two alternate regions on CCM, i.e. PTL fiber contact region and PTL void region. Hence, after deformation CL structure appears to have sinusoidal form, see [67]. To mimic this sinusoidal deformation on CL, mechanical compressive force is assumed to be a sinusoidal with only positive parts and can be projected on the catalyst surface nodes by using a force multiplier between 0 to 1 to the constant increment Δf. By using sinusoidal force multiplier positive parts would imprint PTL fiber and result into PTL contact region. This would create PTL void regions where nodal force

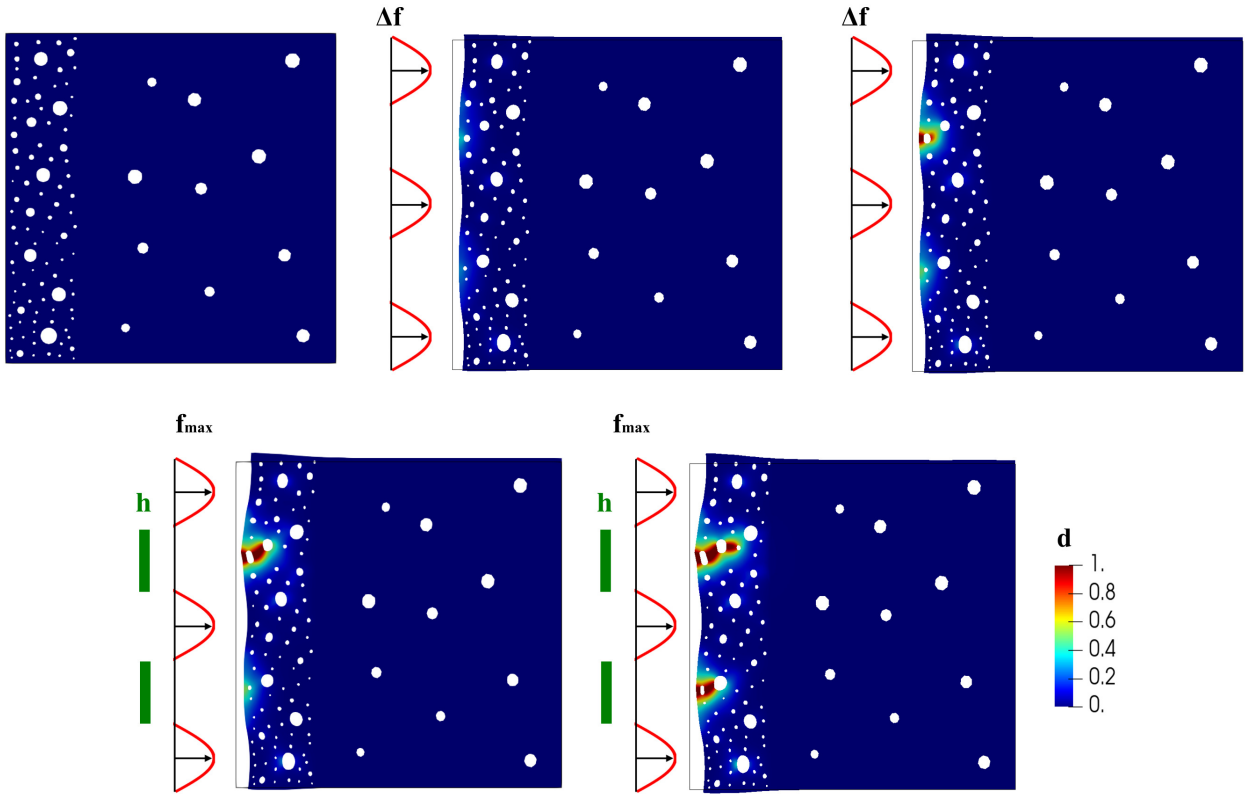

Figure 6: Phase-field evolution due to chemo-mechanically induced fracture on the catalyst coated membrane.

are zero. With this implementation, any PTL structure of given fiber diameter d^{fiber} and pore diameter d^{pore} can be implemented through the change in the amplitude and wavelength of the sinusoidal function, which will change the applied nodal forces on the CCM. Thus, PTL fiber of any diameter and pore size spacing can be implemented. Initial assembled configuration, sinusoidal force multiplier and its implementation are shown in figure 5 (a).

Considering the cell operation, mechanical and chemical boundary conditions are implemented and are plotted in figure 5(b). Mechanical boundary condition of the sinusoidal compressive force is applied with a linear increment of Δf from t_0, until the permitted distortion at force f_{max}. Following that from time t_1, transport of Hydrogen proton with flux h is commenced. Hydrogen flux is applied to only PTL void regions while taking into account alternate stress regions in CL due to compression. For the simplicity, electrode surface coefficient h_0 is considered as a constant flux value $(h(c) = \bar{h}(c) = h_0)$ to implement chemical boundary condition of Hydrogen influx.

As a geometrical setup, we consider a sample square CCM mesh from the PEMWE half cell as shown in figure 5 (c), inspired from [37] for the square geometry dimensions and [90] for the porous representation of the catalyst. It represents a simple microstructure of the anodic side of the CCM specimen in a two-dimensional setting. Herein, catalyst section is employed with denser mesh as compared to the membrane. For the chosen model, geometrical setup is given as: L = 90 μm, Catalyst section = 20 μm, total nodes = 28527, total elements number = 27271 in which catalyst elements are = 25095. According to the mesh size in both regions, length scale parameter is chosen: $ls_{cl} = 1 \times 10^{-3} mm$ for catalyst and $ls_{mem} = 5 \times 10^{-3} mm$ for membrane. Boundary conditions are chosen as follows: Degrees of freedom in the X-direction of all nodes on the right boundary are fixed; X and Y directional degree of freedom of the bottom right node is fixed and force is applied on the left boundary with PTL fiber diameter $d^{fiber} = 11$ μm and pore space $d^{void} = 17.8$ μm taken from low porosity case in [78]. Load increment used for this simulation is $\Delta f = 1 \times 10^{-5} N$. Material and circuit parameters considered for the simulation are according to Table 1. The tolerance used for each sub-algorithm algorithm is $\text{Tol} < 10^{-7}$.

Results of evolution of the phase-field in CCM are demonstrated in figure 6. The black outline box represents the initial configuration of the CCM and it points out the morphological changes of the system with respect to the initial configuration. In figure 6 (left), the catalyst coated membrane is deforming in such a way that it represents the surface of the PTL structure with three fibers imprinted on CCM due to incremental compressive forces. When maximum applied force f_{max} is achieved, crack has formed at the center of top PTL void due to the presence of the high stress along with noticeable damage at the bottom PTL void region, which can be observed figure 6 (middle). This crack initiation is only due to compression forces resulting into alternate tensile and compressive regions in CL. In the next stage, a chemical boundary condition is applied with influx h. Application of the chemical influx has reduced the stress and changed the distribution of compressive and tensile regions in CL, which is coherent with the theory. In this regard, further crack development is observed at void areas. Such crack development is driven by the chemical potential gradients over the CL region. Moreover, damage is noticed near the larger pores within the CL. Remarkable observation from the phase-field evolution is that there are no cracks developed at the PTL contact points and no damage is observed at the MEM region of the CCM. As expected, phase-field is evolved at the PTL void regions due to excess mechanical forces and the continuously increased high chemical potential gradient at the PTL/CL interface.

5.3. BVP2: Fracture of a realistic cathode agglomerate particle

In the second example, we analyse a realistic two-dimensional cathode agglomerate particle. The designed boundary value problem represents crack evolution of the mechanically stressed agglomerate particle due to proton release. For that the geometry and mesh for this BVP are depicted in figure 7. The agglomerate particle edge points are inspired from the SEM micro-graph images of [60; 86; 90; 95; 106]. The outer geometry is formed by a spline approximation of the edge points, where the diameter of surrounding circle of the agglomerate particle in figure 7 is about 300 nm. Plane-strain conditions are assumed for the model problem.

The *previous* mechanical compression loading (stresses) on the agglomerate particle are treated as initial stresses and hence not shown in the evolution. Following this assumption, the agglomerate surface boundary is taken to be displacement and traction free for the mechanical part; whereas proton flux is considered on the chemical part. The initial state of the agglomerate particle is considered as a steady state where the proton concentration equalizes and the agglomerate particle is saturated with Hydrogen protons, see figure 7 (middle). As known, during the operation there exists a sink outside the particle due to the electro-chemical reactions and then the protons move outside leading to the crack initiation and propagation in the agglomerate particle. To this end, the outer surface at the cathodic side is driven by a surface flux $h(c) = \bar{h}(c) = h_0(c - c_{\text{amb}}(t))$ where the ambient concentration is assumed to be decreased

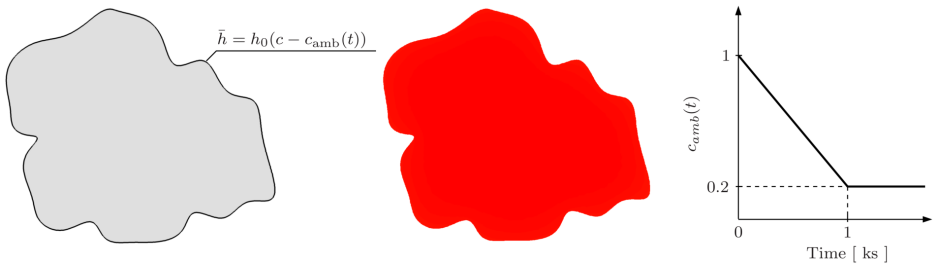

Figure 7: Fracture of a realistic cathode agglomerate particle. Left: geometry and boundary conditions. Middle: Initial steady state, in which the proton concentration equalizes and the particle is saturated with Hydrogen protons. Right: variation of ambient concentration c_{amb} over time.

linearly from $c_{\text{amb}}(0) = 1$ to $c_{\text{amb}} = 0.2$ in order to mimic the sink outside the particle, as depicted in figure 7 (right). In order to ensure a resolution of the fracture phase-field along the crack trajectory, a denser mesh consists of 80000 linear 4-noded $Q1$-elements is employed in the simulation.

Figure 8 demonstrates the crack phase-field d evolution (first-row), the maximum principal Cauchy stress σ_{max} (second-row) and the normalized proton concentration c/c_{max} (third-row) for different loading states until final failure. Initially, the particle is saturated with Hydrogen protons, as outlined in figure 7 (middle). Then, the concentration evolution (in the radially outward direction) starts by application of the flux boundary condition on the outer surface. Due to that, the Hydrogen protons will be released with a concentration gradient in the radial direction, see figure 8 (c1-c4). This proton release increases stresses (s1) on outer surface and accelerates crack initiations (d2). The crack phase-field d starts to evolve when the von Mises stress reaches a critical value (related to the Griffith's fracture energy G_c). Next, the crack tends to propagate in the concentration gradient direction in a rather brittle manner until the region with proton concentration peak is reached, see figure 8 (c3-d3). Then, the crack speed decreases drastically and the

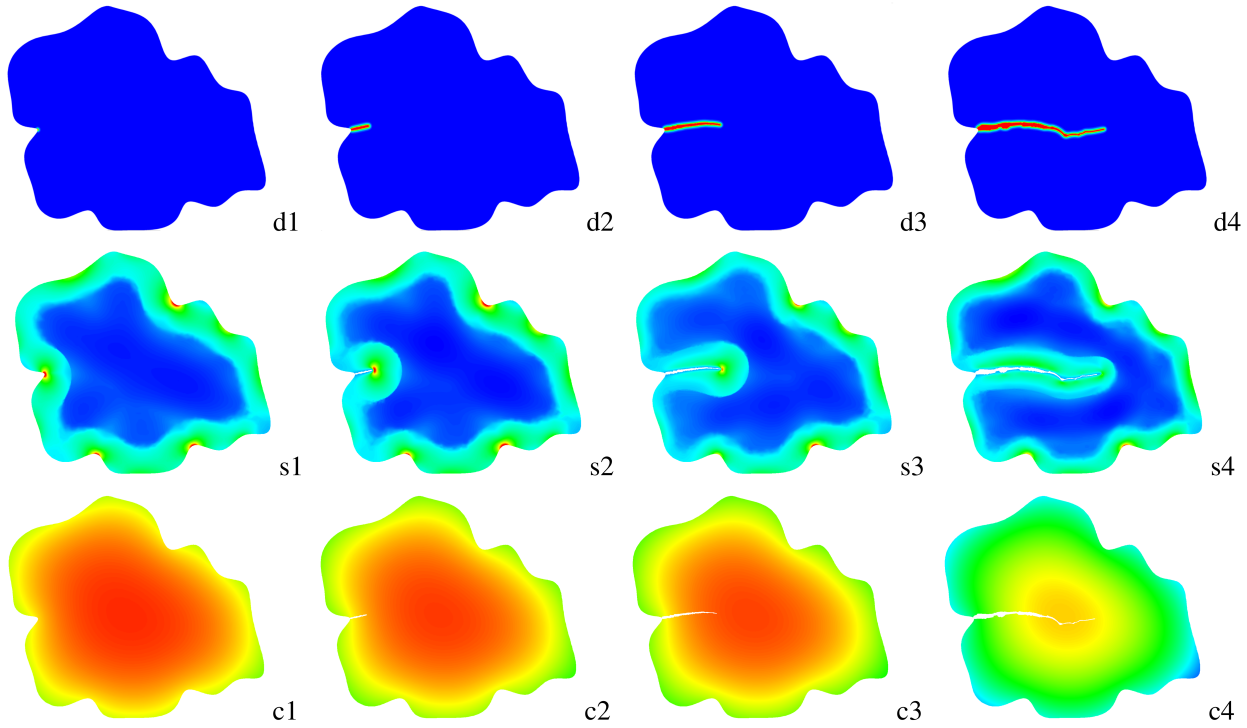

Figure 8: Fracture of a realistic cathode agglomerate particle. (d1-d4) Evolution of the crack phase-field $d \in [0, 1]$; (s1-s4) maximum principal Cauchy stress $\sigma_{\text{max}} \in [0, 0.85\sigma_{cr}]$; and (c1-c4) normalized concentration $c/c_{max} \in [0, 1]$.

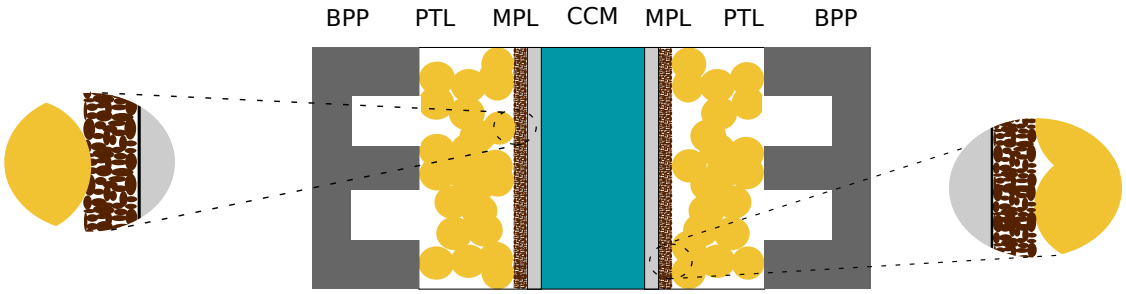

Figure 9: Adding a Microporous layer (MPL) between PTL and CCM to increase the catalyst layer utilization and reduced membrane deformation and crack formation.

crack stabilizes and finally stops. Initially, the crack has an arc shape after the region with highest concentration is reached, it forms a kink where the crack speed is considerably slower than the initial crack speed. The maximum principal stresses driving the crack are given in figure 8 (s1-s4). The crack phase field exceeding a threshold value $d \geq 0.99$ are blanked during post-processing. Prior to crack onset, the principal stresses at several kink points of the agglomerate particle compete. As the crack starts in the kink with highest curvature, the rest of the kinks unload and the stress field changes dramatically. It should be mentioned that the crack initiation is strongly dependent on the topology of the agglomerate particles.

6. Conclusion

In this work, we proposed a theoretical framework and a constitutive model for electro-chemo-mechanically induced fracture in the catalyst area (CL) of the proton exchange membrane water electrolysis (PEMWE) cell. In the computational modeling, we considered a finite strain theory, gradient-extended Cahn-Hillard type diffusion for possible phase separation and a phase-field fracture model. Herein, the electrical coupling was implicitly added by using Butler-Volmer reaction kinetics. To simulate the fracture process in CL at a micrometer length scale, we developed an algorithm in MATLAB based on the constitutive model. Algorithmic decoupling was implemented for the crack evolution with monolithic electro-chemo-mechanical bulk response to provide a less cumbersome method to treat such a complicated problem. Based on the standard experimental cell set up procedure, a boundary value problem was formulated and investigated to track the crack initiation due to mechanical compression and propagation due to electro-chemical reactions in the catalyst layer for anode side half-cell. Another boundary value problem was solved considering realistic cathode particle agglomerate to simulate fracture due to only electro-chemical reactions. These results were in a good agreement with the experimental observations. Investigations of water-splitting reaction mechanism with Cahn-Hillard phase-separation parameters are planned for the future work.

This contribution represents the groundwork for future research to help understand the water splitting and influence of phase separation and its effects on control parameters responsible for the multiphysics problem at the CCM in PEMWE cells. Open challenges for the future direction are: (i) to prepare the mesh that represents the real microstructure of the CCM; (ii) to extract real material and control parameters for Hydrogen diffusion (iii) the extra computational cost; (iv) to improve the PEM water electrolysis cell performance in terms of mass and electron transport by developing a microporous layer (MPL) between the standard PTL and CCM layers (figure 9). This could be accomplished by using nanostructured fillers or dopers with high electron conductivity and high corrosion resistance, in line with [79]. All these challenges will be investigated in future works.

Acknowledgment. The corresponding author Fadi Aldakheel (FA) appreciates the scientific support of the subproject C4 within the Deutsche Forschungsgemeinschaft (**DFG**, German Research Foundation) in the Collaborative Research Center **CRC 1153** (Project ID 252662854). FA would like to thank Prof. **Peter Wriggers** (LUH Hannover) and Dr. **Michel Suermann** (LUH Hannover, meanwhile with Siemens Energy) for the fruitful discussions and comments. RHR and BB gratefully acknowledge the financial support by the **Federal Ministry of Economic Affairs and Climate Action of Germany in the framework of HoKaWe** (Project ID 03EI3029B).

References

[1] Abali, B. E., Aldakheel, F., & Zohdi, T. I. (2022). Multiphysics computation of thermomechanical fatigue in electronics under electrical loading. In *Current Trends and Open Problems in Computational Mechanics* (pp. 1–14). Springer.

[2] Ahmet, K. (2018). Ionomer thin films in pem fuel cells. In *Encyclopedia of Sustainability Science and Technology* (pp. 1–23). Springer New York.

[3] Aldakheel, F. (2016). *Mechanics of Nonlocal Dissipative Solids: Gradient Plasticity and Phase Field Modeling of Ductile Fracture*. Ph.D. thesis Institute of Applied Mechanics (CE), Chair I, University of Stuttgart. Http://dx.doi.org/10.18419/opus-8803.

[4] Aldakheel, F. (2020). A microscale model for concrete failure in poro-elasto-plastic media. *Theoretical and Applied Fracture Mechanics*, *107*, 102517.

[5] Aldakheel, F., Noii, N., Wick, T., Allix, O., & Wriggers, P. (2021). Multilevel global–local techniques for adaptive ductile phase-field fracture. *Computer Methods in Applied Mechanics and Engineering*, *387*, 114175.

[6] Aldakheel, F., Satari, R., & Wriggers, P. (2021). Feed-forward neural networks for failure mechanics problems. *Applied Sciences*, *11*, 6483.

[7] Alessi, R., Freddi, F., & Mingazzi, L. (2020). Phase-field numerical strategies for deviatoric driven fractures. *Computer Methods in Applied Mechanics and Engineering*, *359*, 112651.

[8] Alessi, R., Marigo, J.-J., Maurini, C., & Vidoli, S. (2017). Coupling damage and plasticity for a phase-field regularisation of brittle, cohesive and ductile fracture: One-dimensional examples. *International Journal of Mechanical Sciences*, . Https://doi.org/10.1016/j.ijmecsci.2017.05.047.

[9] Ali, B., Heider, Y., & Markert, B. (2021). Residual stresses in gas tungsten arc welding: a novel phase-field thermo-elastoplasticity modeling and parameter treatment framework. *Computational Mechanics*, (pp. 1–23).

[10] Ambati, M., Gerasimov, T., & De Lorenzis, L. (2015). Phase-field modeling of ductile fracture. *Computational Mechanics*, *55*, 1017–1040.

[11] Ambati, M., Heinzmann, J., Seiler, M., & Kästner, M. (2022). Phase-field modelling of brittle fracture along the thickness direction of plates and shells. *International Journal for Numerical Methods in Engineering*, . Https://doi.org/10.1002/nme.7001.

[12] Anand, L. (2012). A cahn-hilliard-type theory for species diffusion coupled with large elastic-plastic deformations. *Journal of the Mechanics and Physics of Solids*, *60*, 1983–2002.

[13] Arash, B., Exner, W., & Rolfes, R. (2021). A finite deformation phase-field fracture model for the thermo-viscoelastic analysis of polymer nanocomposites. *Computer Methods in Applied Mechanics and Engineering*, *381*, 113821.

[14] Arico, A. S., Siracusano, S., Briguglio, N., Baglio, V., Blasi, A. D., & Antonucci, V. (2013). Polymer electrolyte membrane water electrolysis: status of technologies and potential applications in combination with renewable power sources. *J Appl Electrochem*, *43*, 107–118.

[15] Babic, U. (2019). *Polymer electrolyte water electrolysis: Development of diagnostics methods and mitigation strategies to tackle component degradation*. Ph.D. thesis ETH Zurich.

[16] Babic, U., Nilsson, E., Pătru, A., Schmidt, T. J., & Gubler, L. (2019). Proton transport in catalyst layers of a polymer electrolyte water electrolyzer: Effect of the anode catalyst loading. *Journal of The Electrochemical Society*, *166*, F214–F220.

[17] Babic, U., Schmidt, T. J., & Gubler, L. (2018). Communication—contribution of catalyst layer proton transport resistance to voltage loss in polymer electrolyte water electrolyzers. *Journal of The Electrochemical Society*, *165*, J3016–J3018.

[18] Babic, U., Tarik, M., Schmidt, T. J., & Gubler, L. (2020). Understanding the effects of material properties and operating conditions on component aging in polymer electrolyte water electrolyzers. *Journal of Power Sources*, *451*, 227778.

[19] Bharali, R., Larsson, F., & Jänicke, R. (2021). Computational homogenisation of phase-field fracture. *European Journal of Mechanics-A/Solids*, *88*, 104247.

[20] Bourdin, B., Francfort, G., & Marigo, J.-J. (2008). The variational approach to fracture. *Journal of Elasticity*, *91*, 5–148.

[21] Bryant, E. C., & Sun, W. (2021). Phase field modeling of frictional slip with slip weakening/strengthening under non-isothermal conditions. *Computer Methods in Applied Mechanics and Engineering*, *375*, 113557.

[22] Bueler, M., Hegge, F., Holzapfel, P., & Bierling, M. (2019). Optimization of anodic porous transport electrodes for proton exchange membrane water electrolyzers. *Journals of Material Chemistry A*, *7*, 26984–26995.

[23] Carmo, M., Fritz, D., Mergel, J., & Stolten, D. (2013). A comprehensive review on pem water electrolysis. *International Journal of Hydrogen Energy*, *38*, 4901–4934.

[24] Choo, J., & Sun, W. (2018). Coupled phase-field and plasticity modeling of geological materials: From brittle fracture to ductile flow. *Computer Methods in Applied Mechanics and Engineering*, *330*, 1–32.

[25] Cui, C., Ma, R., & Martínez-Pañeda, E. (2022). A generalised, multi-phase-field theory for dissolution-driven stress corrosion cracking and hydrogen embrittlement. *Journal of the Mechanics and Physics of Solids*, (p. 104951).

[26] Dal, H., & Miehe, C. (2015). Computational electro-chemo-mechanics of lithium-ion battery electrodes at finite strains. *Comput Mech*, *55*, 303–325.

[27] De Angelis, S., Schuler, T., Charalambous, M. A., Marone, F., Schmidt, T. J., & Büchi, F. N. (2021). Unraveling two-phase transport in porous transport layer materials for polymer electrolyte water electrolysis. *J. Mater. Chem. A*, *9*, 22102–22113.

[28] Dean, A., Reinoso, J., Jha, N., Mahdi, E., & Rolfes, R. (2020). A phase field approach for ductile fracture of short fibre reinforced composites. *Theoretical and Applied Fracture Mechanics*, (p. 102495). Https://doi.org/10.1016/j.tafmec.2020.102495.

[29] Dehghan, M., & Gharibi, Z. (2021). Numerical analysis of fully discrete energy stable weak galerkin finite element scheme for a coupled cahn-hilliard-navier-stokes phase-field model. *Applied Mathematics and Computation*, *410*, 126487.

[30] Denli, F. A., Gültekin, O., Holzapfel, G. A., & Dal, H. (2020). A phase-field model for fracture of unidirectional fiber-reinforced polymer matrix composites. *Computational Mechanics*, *65*, 1149–1166.

[31] Dominković, D. F., Bačeković, I., Ćosić, B., Krajačić, G., Pukšec, T., Duić, N., & Markovska, N. (2016). Zero carbon energy system of south east europe in 2050. *Applied energy*, *184*, 1517–1528.

[32] Fang, J., Wu, C., Li, J., Liu, Q., Wu, C., Sun, G., & Li, Q. (2019). Phase field fracture in elasto-plastic solids: Variational formulation for multi-surface plasticity and effects of plastic yield surfaces and hardening. *International Journal of Mechanical Sciences*, *156*, 382–396.

[33] Fantoni, F., Bacigalupo, A., Paggi, M., & Reinoso, J. (2019). A phase field approach for damage propagation in periodic microstructured materials. *International Journal of Fracture*, (pp. 1–24).

[34] Fimrite, J., Struchtrup, H., & Djilali, M. (2005). Transport phenomena in polymer electrolyte membranes i. modelling framework. *Journals of the Electrochemical Society*, *152 A*, 1804–1814.

[35] Garbe, S., Babic, U., Nilsson, E., Schmidt, T. J., & Gubler, L. (2019). Communication—pt-doped thin membranes for gas crossover suppression in polymer electrolyte water electrolysis. *Journal of The Electrochemical Society*, *166*, F873–F875.

[36] Grigoriev, S., Kalinnikov, A., Millet, P., Porembsky, V., & Fateev, V. (2010). Mathematical modeling of high-pressure pem water electrolysis. *J Appl Electrochem*, *40*, 921–932.

[37] Hegge, F., Moroni, R., Trinke, P., Bensmann, B., Hanke-Rauschenbach, R., Thiele, S., & Vierrath, S. (2018). Three-dimensional microstructure analysis of a polymer electrolyte membrane water electrolyzer anode. *Journal of Power Sources*, *393*, 62–66.

[38] Heider, Y. (2021). Multi-field and multi-scale computational fracture mechanics and machine-learning material modeling, . Https://publications.rwth-aachen.de/record/835190.

[39] Heider, Y. (2021). A review on phase-field modeling of hydraulic fracturing. *Engineering Fracture Mechanics*, *253*, 107881.

[40] Heider, Y., Bamer, F., Ebrahem, F., & Markert, B. (2022). Self-organized criticality in fracture models at different scales. *Examples and Counterexamples*, *2*, 100054.

[41] Heister, T., Wheeler, M. F., & Wick, T. (2015). A primal-dual active set method and predictor-corrector mesh adaptivity for computing fracture propagation using a phase-field approach. *Computer Methods in Applied Mechanics and Engineering*, *290*, 466 – 495.

[42] Hesch, C., & Weinberg, K. (2014). Thermodynamically consistent algorithms for a finite-deformation phase-field approach to fracture. *International Journal for Numerical Methods in Engineering*, *99*, 906–924.

[43] Immerz, C., Bensmann, B., & Hanke-Rauschenbach, R. (2021). Model-based analysis of low stoichiometry operation in proton exchange membrane water electrolysis. *Membranes*, *11*.

[44] Immerz, C., Bensmann, B., Trinke, P., Suermann, M., & Hanke-Rauschenbach, R. (2018). Local current density and electrochemical impedance measurements within 50 cm single-channel pem electrolysis cell. *Journal of the Electrochemical Society*, *165*.

[45] Immerz, C., Bensmann, B., Trinke, P., Suermann, M., & Hanke-Rauschenbach, R. (2019). Understanding electrical under- and overshoots in proton exchange membrane water electrolysis cells. *Journal of The Electrochemical Society*, *161*.

[46] Ito, H., Maeda, T., Nakano, A., & Takenaka, H. (2011). Properties of nafion membranes under pem water electrolysis conditions. *International journal of Hydrogen energy*, *36*, 527–540.

[47] Khalil, Z., Elghazouli, A. Y., & Martínez-Pañeda, E. (2022). A generalised phase field model for fatigue crack growth in elastic–plastic solids with an efficient monolithic solver. *Computer Methods in Applied Mechanics and Engineering*, *388*, 114286.

[48] Krüger, M., Dittmann, M., Aldakheel, F., Härtel, A., Wriggers, P., & Hesch, C. (2019). Porous-ductile fracture in thermo-elasto-plastic solids with contact applications. *Computational Mechanics*, (pp. 1–26). Https://doi.org/10.1007/s00466-019-01802-3.

[49] Leo, C. V. D., Rejovitzky, E., & anand, L. (2014). A cahn-hilliard-type phase-field theory for species diffusion coupled with large elastic deformations: Application to phase-separating li-ion materials. *Journal of the Mechanics and Physics of Solids*, .

[50] Liso, V., Savoia, G., Araya, S., Cinti, G., & Kaer, S. (2018). Modelling and experimental analysis of a polymer electrolyte membrane water electrolysis cell at different operating temperatures. *Energies*, *11*.

[51] Martin, A., Trinke, P., Pham, C. V., Bühler, M., Bierling, M., Holzapfel, P. K. R., Bensmann, B., Thiele, S., , & Hanke-Rauschenbach, R. (2021). On the correlation between the oxygen in hydrogen content and the catalytic activity of cathode catalysts in pem water electrolysis. *Journal of the Electrochemical Society*, *168*.

[52] Martin, A., Trinke, P., Stähler, M., Stähler, A., Scheepers, F., Bensmann, B., Carmo, M., Lehnert, W., & Hanke-Rauschenbach, R. (2022). The effect of cell compression and cathode pressure on hydrogen crossover in pem water electrolysis. *Journal of the Electrochemical Society*, *169*.

[53] Martínez-Pañeda, E., Golahmar, A., & Niordson, C. F. (2018). A phase field formulation for hydrogen assisted cracking. *Computer Methods in Applied Mechanics and Engineering*, *342*, 742–761.

[54] Miehe, C., Dal, H., Schänzel, L.-M., & Raina, A. (2016). A phase-field model for chemo-mechanical induced fracture in lithium-ion battery electrode particles. *International Journal for Numerical Methods in Engineering*, *106*, 683–711.

[55] Miehe, C., Hildebrand, F. E., & Boeger, L. (2014). Mixed variational potentials and inherent symmetries of the cahn-hilliard theory of diffusive phase separation. *Proceeding of Royal Society A*, *470*.

[56] Miehe, C., Hofacker, M., Schänzel, L.-M., & Aldakheel, F. (2015). Phase field modeling of fracture in multi-physics problems. Part II. brittle-to-ductile failure mode transition and crack propagation in thermo-elastic-plastic solids. *Computer Methods in Applied Mechanics and Engineering*, *294*, 486–522.

[57] Miehe, C., Mauthe, S., & Teichtmeister, S. (2015). Minimization principles for the coupled problem of darcy-biot-type fluid transport in porous media linked to phase field modeling of fracture. *Journal of the Mechanics and Physics of Solids*, .

[58] Miehe, C., Mauthe, S., & Ulmer, H. (2014). Formulation and numerical exploitation of mixed variational principles for coupled problems of cahn-hilliard-type and standard diffusion in elastic solids. *International journal for numerical methods in engineering*, *99*, 737–762.

[59] Miehe, C., Welschinger, F., & Hofacker, M. (2010). Thermodynamically consistent phase-field models of fracture: Variational principles and multi-field FE implementations. *International Journal for Numerical Methods in Engineering*, *83*, 1273–1311.

[60] Millet, P. (2015). 9 - hydrogen production by polymer electrolyte membrane water electrolysis. In V. Subramani, A. Basile, & T. N. Veziroğlu (Eds.), *Compendium of Hydrogen Energy* Woodhead Publishing Series in Energy (pp. 255–286). Oxford: Woodhead Publishing.

[61] Millet, P., Ngameni, R., Grigoriev, S., Mbemba, N., Brisset, F., Ranjbari, A., & Etiévant, C. (2010). Pem water electrolyzers: From electrocatalysis to stack development. *International Journal of hydrogen energy*, *35*, 5043–5052.

[62] Mohammadi, V., & Dehghan, M. (2020). A meshless technique based on generalized moving least squares combined with the second-order semi-implicit backward differential formula for numerically solving time-dependent phase field models on the spheres. *Applied Numerical Mathematics*, *153*, 248–275.

[63] Nguyen, L. H., & Schillinger, D. (2019). The multiscale finite element method for nonlinear continuum localization problems at full fine-scale fidelity, illustrated through phase-field fracture and plasticity. *Journal of Computational Physics*, *396*, 129–160.

[64] Noii, N., Khodadadian, A., & Aldakheel, F. (2022). Probabilistic failure mechanisms via monte carlo simulations of complex microstructures. *Computer Methods in Applied Mechanics and Engineering*, *399*, 115358.
[65] Noii, N., Khodadadian, A., Ulloa, J., Aldakheel, F., Wick, T., François, S., & Wriggers, P. (2021). Bayesian inversion for unified ductile phase-field fracture. *Computational Mechanics*, *68*, 943–980.
[66] Noii, N., Khodadadian, A., Ulloa, J., Aldakheel, F., Wick, T., François, S., & Wriggers, P. (2022). Bayesian inversion with open-source codes for various one-dimensional model problems in computational mechanics. *Archives of Computational Methods in Engineering*, (pp. 1–34).
[67] Papakonstantinou, G., Algara-Siller, G., Teschner, D., Vidaković-Koch, T., Schlögl, R., & Sundmacher, K. (2020). Degradation study of a proton exchange membrane water electrolyzer under dynamic operation conditions. *Applied Energy*, *280*, 115911.
[68] Pillai, U., Triantafyllou, S. P., Essa, Y., & de la Escalera, F. M. (2020). An anisotropic cohesive phase field model for quasi-brittle fractures in thin fibre-reinforced composites. *Composite Structures*, *252*, 112635.
[69] Quaschning, V. V. (2019). *Renewable energy and climate change*. John Wiley & Sons.
[70] Rezaei, S., Harandi, A., Brepols, T., & Reese, S. (2022). An anisotropic cohesive fracture model: advantages and limitations of length-scale insensitive phase-field damage models. *Engineering Fracture Mechanics*, (p. 108177).
[71] Rezaei, S., Mianroodi, J. R., Brepols, T., & Reese, S. (2021). Direction-dependent fracture in solids: Atomistically calibrated phase-field and cohesive zone model. *Journal of the Mechanics and Physics of Solids*, *147*, 104253.
[72] Rozian, C., & P.Millet (2014). Electrochemical characterization of polymer electrolyte membrane water electrolysis cells. *Electrochemica Acta*, *131*, 160–167.
[73] Sai, K., & Sandip, M. (2008). Computational modeling of the cathode catalyst layer of a pemfc, . *Heat Transfer: Volume 3*, 581–590.
[74] Sai, K., & Sandip, M. (2012). Cathode catalyst layer model for polymer electrolyte membrane fuel cell, . *Volume 6: Energy, Parts A and B*, 789–798.
[75] Schmidt, G., Suermann, M., Bensmann, B., & R. Hanke-Rauschenbach, I. N. (2020). Modeling overpotentials related to mass transport through porous transport layers of pem water electrolysis cells. *Journal of The Electrochemical Society*, *166*.
[76] Schreiber, C., Kuhn, C., Müller, R., & Zohdi, T. (2020). A phase field modeling approach of cyclic fatigue crack growth. *International Journal of Fracture*, *225*, 89–100.
[77] Schröder, J., Pise, M., Brands, D., Gebuhr, G., & Anders, S. (2022). Phase-field modeling of fracture in high performance concrete during low-cycle fatigue: Numerical calibration and experimental validation. *Computer Methods in Applied Mechanics and Engineering*, *398*, 115181.
[78] Schuler, T., Bruycker, R., Schmidt, T., & Büchi, F. (2019). Polymer electrolyte water electrolysis: Correlating porous transport layer structural properties and performance: Part i. tomographic analysis of morpholoy and topology. *Journal of The Electrochemical Society*, *166*, F270–F281.
[79] Schuler, T., Ciccone, J. M., Krentscher, B., Marone, F., Peter, C., Schmidt, T. J., & Büchi, F. N. (2020). Hierarchically structured porous transport layers for polymer electrolyte water electrolysis. *Advanced Energy Materials*, *10*, 1903216.
[80] Schuler, T., Schmidt, T., & Buechi, F. (2019). Polymer electrolyte water electrolysis: Correlating performance and porous transport layer structure: Part ii. electrochemical performance analysis. *Journal of The Electrochemical Society*, *166*, F555–F565.
[81] Seiler, M., Keller, S., Kashaev, N., Klusemann, B., & Kästner, M. (2021). Phase-field modelling for fatigue crack growth under laser shock peening-induced residual stresses. *Archive of Applied Mechanics*, *91*, 3709–3723.
[82] Seleš, K., Aldakheel, F., Tonković, Z., Sorić, J., & Wriggers, P. (2021). A general phase-field model for fatigue failure in brittle and ductile solids. *Computational Mechanics*, *67*, 1431–1452.
[83] Shanthraj, P., Sharma, L., Svendsen, B., Roters, F., & Raabe, D. (2016). A phase field model for damage in elasto-viscoplastic materials. *Computer Methods in Applied Mechanics and Engineering*, *312*, 167–185.
[84] Shiva Kumar, S., & Himabindu, V. (2019). Hydrogen production by pem water electrolysis – a review. *Materials Science for Energy Technologies*, *2*, 442–454.
[85] Sibbing, Z. (2015). *Bachelor Thesis: Numerical methods for the implementation of the Cahn-Hilliard equation in one dimension and dynamic boundary condition in two dimensions*. Delft University of Technology.
[86] Siracusano, S., Trocino, S., Briguglio, N., Pantó, F., & Aricó, A. S. (2020). Analysis of performance degradation during steady-state and load-thermal cycles of proton exchange membrane water electrolysis cells. *Journal of Power Sources*, *468*.
[87] Springer, T. E., Zawodzinski, T. A., & Gottesfeld, S. (1991). Polymer electrolyte fuel cell model. *Journal of The Electrochemical Society*, *138*, 2334–2342.
[88] Steinke, C., & Kaliske, M. (2019). A phase-field crack model based on directional stress decomposition. *Computational Mechanics*, *63*, 1019–1046.
[89] Storm, J., Pise, M., Brands, D., Schröder, J., & Kaliske, M. (2021). A comparative study of micro-mechanical models for fiber pullout behavior of reinforced high performance concrete. *Engineering Fracture Mechanics*, *243*, 107506.
[90] Suter, T. A. M., Smith, K., Hack, J., Rasha, L., Rana, Z., Angel, G. M. A., Shearing, P. R., Miller, T. S., & Brett, D. J. L. (2021). Engineering catalyst layers for next-generation polymer electrolyte fuel cells: A review of design, materials, and methods. *Advanced Engineering Materials*, *11*.
[91] Tan, W., & Martínez-Pañeda, E. (2022). Phase field fracture predictions of microscopic bridging behaviour of composite materials. *Composite Structures*, *286*, 115242.
[92] Tanaka, Y., Kikuchi, K., Saihara, Y., & Ogumi, Z. (2005). Bubble visualization and electrolyte dependency of dissolving hydrogen in electrolyzed water using solid-polymer-electrolyte. *Electrochimica Acta*, *50*, 5229–5236. Electrochemistry: from Nanostructures to Power Plants.
[93] Tanaka, Y., Uchinashi, S., Saihara, Y., Kikuchi, K., Okaya, T., & Ogumi, Z. (2003). Dissolution of hydrogen and the ratio of the dissolved hydrogen content to the produced hydrogen in electrolyzed water using spe water electrolyzer. *Electrochimica Acta*, *48*, 4013–4019.
[94] `climateactiontracker.org` (2021). Https://climateactiontracker.org/countries/eu/.
[95] Trinke, P. (2021). *Experimental and Model-based Investigations on Gas Crossover in Polymer Electrolyte Membrane Water Electrolyzers*.

Ph.D. thesis Gottfried Wilhelm Leibniz Universität Hannover.

[96] Trinke, P., Keeley, G. P., Carmo, M., Bensmann, B., & Hanke-Rauschenbach, R. (2019). Elucidating the effect of mass transport resistances on hydrogen crossover and cell performance in PEM water electrolyzers by varying the cathode ionomer content. *Journal of The Electrochemical Society*, *166*, F465–F471.

[97] Ugljesa, B., Suermann, M., Büchi, F. N., Gubler, L., & Schmidt, T. J. (2017). Critical review—identifying critical gaps for polymer electrolyte water electrolysis development. *Journal of The Electrochemical Society*, *164*, F387.

[98] Ulloa, J., Noii, N., Alessi, R., Aldakheel, F., Degrande, G., & François, S. (2022). Variational modeling of hydromechanical fracture in saturated porous media: A micromechanics-based phase-field approach. *Computer Methods in Applied Mechanics and Engineering*, *396*, 115084.

[99] Ursua, A., Gandia, L., & Sanchis, P. (2012). Hydrogen production from water electrolysis: Current status and future trends. *Proceedings of the IEE*, *100*.

[100] Wick, T. (2020). *Multiphysics Phase-Field Fracture: Modeling, Adaptive Discretizations, and Solvers*. De Gruyter.

[101] Wriggers, P. (2008). *Nonlinear Finite Element Methods*. Springer.

[102] Wu, T., & Lorenzis, L. D. (2016). A phase-field approach to fracture coupled with diffusion. *Comput. Methods Appl. Mech. Engrg*, *312*, 196–223.

[103] Yin, B., Zhao, D., Storm, J., & Kaliske, M. (2022). Phase-field fracture incorporating cohesive adhesion failure mechanisms within the representative crack element framework. *Computer Methods in Applied Mechanics and Engineering*, *392*, 114664.

[104] Yin, Y., Li, R., Bai, F., Zhu, W., Qin, Y., Chang, Y., Zhang, J., & Guiver, M. D. (2019). Ionomer migration within pemfc catalyst layers induced by humidity changes. *Electrochemistry Communications*, *109*, 106590.

[105] Yu, H., Bonville, L., Jankovic, J., & Maric, R. (2020). Microscopic insights on the degradation of a pem water electrolyzer with ultra-low catalyst loading. *Applied Catalysis B-environmental*, *260*, 118194.

[106] Yu, K., Groom, D. J., Wang, X., Yang, Z., Gummalla, M., Ball, S. C., Myers, D. J., & Ferreira, P. J. (2014). Degradation mechanisms of platinum nanoparticle catalysts in proton exchange membrane fuel cells: The role of particle size. *Chemistry of Materials*, *26*, 5540–5548.

[107] Zhuang, X., Zhou, S., Huynh, G., Aerias, P., & Rabczuk, T. (2022). Phase field modelling and computer implementation: A review. *Engineering Fracture Mechanics*, (p. 108234).

[108] Zohdi, T. (2004). Modeling and simulation of a class of coupled thermo-chemo-mechanical processes in multiphase solids. *Computer methods in applied mechanics and engineering*, *193*, 679–699.

[109] Zohdi, T. (2010). Simulation of coupled microscale multiphysical-fields in particulate-doped dielectrics with staggered adaptive fdtd. *Computer Methods in Applied Mechanics and Engineering*, *199*, 3250–3269.

[110] Zohdi, T., & Meletis, E. (1998). Calculation of hydrogen buildup in the neighborhood of intergranular cracks. *Journal of the Mechanical Behavior of Materials*, *9*, 23–34.

[111] Zohdi, T., & Wriggers, P. (2000). Phenomenological modeling and numerical simulation of the environmental degradation of multiphase engineering materials. *Archive of Applied Mechanics*, *70*, 47–64.